

Thermodynamic Limit in Learning Period Three

Yuichiro Terasaki^{1,*} and Kohei Nakajima^{2,3,†}

¹*Department of Mechano-Informatics, The University of Tokyo, Tokyo 113-8656, Japan*

²*Graduate School of Information Science and Technology,
The University of Tokyo, Tokyo 113-8656, Japan*

³*Next Generation Artificial Intelligence Research Center,
The University of Tokyo, Tokyo 113-8656, Japan*

(Dated: May 16, 2024)

A continuous one-dimensional map with period three includes all periods. This raises the following question: Can we obtain any types of periodic orbits solely by learning three data points? We consider learning period three with random neural networks and report the universal property associated with it. We first show that the trained networks have a thermodynamic limit that depends on the choice of target data and network settings. Our analysis reveals that almost all learned periods are unstable and each network has its characteristic attractors (which can even be untrained ones). Here, we propose the concept of characteristic bifurcation expressing embeddable attractors intrinsic to the network, in which the target data points and the scale of the network weights function as bifurcation parameters. In conclusion, learning period three generates various attractors through characteristic bifurcation due to the stability change in latently existing numerous unstable periods of the system.

With the advent of reservoir computing (RC) [1], which exploits the dynamics of high-dimensional dynamical systems for learning, many interesting properties of random networks have been discovered from a dynamical systems perspective. For example, with a fixed-weight random recurrent neural network, the so-called echo-state network (ESN) [2]—as a reservoir—we can create an autonomous system that emulates target chaotic systems by simply fitting its readout layer [3, 4]. Such an attractor-embedding ability is linked to the existence of the generalized synchronization between an input dynamical system and a reservoir [4–7]. In addition, recent studies have revealed that RC can simultaneously embed multiple attractors [8] and may have untrained attractors that are not part of the training data [8–12]. Surprisingly, a successful reservoir computer only needs a few pairs of bifurcation parameter values and corresponding trajectories to reconstruct the entire bifurcation structure of a target system [10, 11]. These properties are valuable, for example, in the context of robot locomotion control using dynamical system attractors that can significantly reduce the training data [13–15]. Thus, the powerful generalization and multifunctionality aspects of RC are related to the dynamical systems properties of a learning machine.

In one-dimensional discrete dynamical systems, there are two significant theorems on periodic orbits [16–18]:

Theorem 1 (Sharkovsky) *If a continuous map $f : I \rightarrow I$ has a periodic point of period m and $m \succ n$, then f also has a periodic point of period n .*

Theorem 2 (Li–Yorke) *If a continuous map $f : I \rightarrow I$ has a point $a \in I$ for which the points $b = f(a)$, $c = f(f(a))$, and $d = f(f(f(a)))$ satisfy*

$$d \leq a < b < c \quad (\text{or} \quad d \geq a > b > c),$$

then f has a periodic point of period k for every $k \in \mathbb{N}$.

Note that the interval I does not need to be closed or bounded. Here, the ordering of positive integers \succ in Theorem 1 is called the Sharkovsky ordering and is given below:

$$\begin{aligned} 3 \succ 5 \succ 7 \succ 9 \succ \dots \succ 2 \cdot 3 \succ 2 \cdot 5 \succ 2 \cdot 7 \succ \dots \\ \succ 2^2 \cdot 3 \succ 2^2 \cdot 5 \succ 2^2 \cdot 7 \succ \dots \succ 2^3 \succ 2^2 \succ 2 \succ 1. \end{aligned} \quad (1)$$

We write $m \succ n$ whenever m is to the left of n in Eq. (1). As a consequence of both theorems, a continuous one-dimensional map with period three has all periods. We note that such a map also has an uncountable set containing no (asymptotically) periodic points, the so-called scrambled set, and is chaotic in the sense of Li–Yorke [18].

Now, the following natural question arises: Can we obtain all the periods in the network through training only period three? If we successfully train period three in one-dimensional dynamics, then the straightforward answer is “yes.” However, this question is somewhat naive, since the above theorems do not reveal whether the obtained periods are stable. Instead, we should ask the following question: Which kind of stable orbits (attractors) can we obtain by learning period three? This paper is devoted to theoretically answer this question in terms of all aspects. Here, we consider training readout weights of a two-layer random feedforward neural network to learn period three [19–22]: $f_N(x) \equiv \frac{1}{\sqrt{N}} \sum_{i=1}^N W_i^{\text{out}} \phi(h_i(x))$, $h_i(x) \equiv W_i^{\text{in}} x + b_i^{\text{in}}$, where $x \in \mathbb{R}$ is an input of the network, $W^{\text{in}} \in \mathbb{R}^{N \times 1}$ and $b^{\text{in}} \in \mathbb{R}^N$ are the input weights and biases, respectively, randomly drawn from a Gaussian distribution with zero mean and variance given by σ^2 , $\phi : \mathbb{R} \rightarrow \mathbb{R}$ is an activation function, and $W^{\text{out}} \in \mathbb{R}^{1 \times N}$ is the output weights matrix optimized

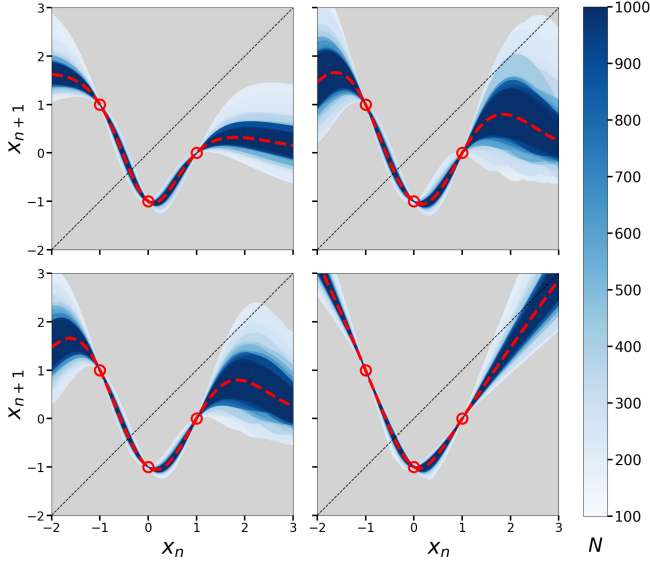


FIG. 1. Trained maps f_N^* for activation functions $\phi = \text{erf}$ (top left), \sin (top right), \cos (bottom left), and ReLU (bottom right), with target period three $\mathcal{D} = \{-1, 1, 0\}$ and input intensity $\sigma = 1.0$. The blue-colored areas indicate the maximum–minimum regions of f_N^* for 100 different realizations. The red circles and the red dotted lines show \mathcal{D} and the thermodynamic limit f_∞^* , respectively. The darkness of blue corresponds to the number of nodes N , describing that f_N^* degenerates into f_∞^* as N increases.

by a learning method described subsequently (see Sec. I in the Supplementary Material [23] for the other network settings and detailed derivations, which includes Refs. [24–26]). We denote the trained network output by $f_N^*(x)$ and call σ the input intensity. Hereafter, we consider the following specific activation functions: bounded and smooth $\phi = \text{erf}, \sin, \cos$ and unbounded and non-smooth $\phi = \text{ReLU}$. Actually, this model can be regarded as a special case of an ESN in which the spectral radius of the adjacency matrix is zero. With the trained network f_N^* , we study the dynamical system $x_{n+1} = f_N^*(x_n)$ created from a closed loop that connects its input and output. The attractors of f_N^* should depend on the network structure, including the realizations of W^{in} and b^{in} and the choice of ϕ , which makes the above question non-trivial.

Our findings are twofold. First, concerning general training data, we show that the trained map f_N^* degenerates into its thermodynamic limit f_∞^* as N increases (Fig. 1) based on the neural tangent kernel (NTK) theory [27, 28] under certain assumptions. Second, in learning period three, we reveal that in contrast to our expectation, almost all acquired periods are unstable; it has characteristic attractors corresponding to the choice of target period three, nonlinearity ϕ , and input intensity σ . Interestingly, the changes in the target data points and σ , which can be regarded as controllable system param-

eters, cause the bifurcation of the characteristic attractors, enabling learning machines to embed a diverse range of dynamics in their bifurcation structure. We discuss the range of applicability of our proposed approach toward physical learning machines at the end of this paper.

We denote the training dataset and its number by $\mathcal{D} \subseteq \mathbb{R} \times \mathbb{R}$ and $|\mathcal{D}|$, respectively, and assume $N \geq |\mathcal{D}|$. We use \mathcal{X} and \mathcal{Y} vectors to denote the input and output data and define them as $\mathcal{X} \equiv [x_1, \dots, x_{|\mathcal{D}|}]$, $\mathcal{Y} \equiv [y_1, \dots, y_{|\mathcal{D}|}] \in \mathbb{R}^{|\mathcal{D}|}$, where $(x_i, y_i) \in \mathcal{D}$. In learning period three ($a \mapsto b \mapsto c \mapsto a \mapsto \dots$), the target input–output pairs are $\mathcal{D} = \{(a, b), (b, c), (c, a)\}$, $\mathcal{X} = [a, b, c]$, and $\mathcal{Y} = [b, c, a]$. For the sake of simplicity, we write $\mathcal{D} = \{a, b, c\}$ and assume $a < b$. Note that a period-3 orbit is of two types: $\{a, b, c\}$ and $\{b, a, c\}$. Generally, a period- n orbit has $(n-1)!$ types. For a given \mathcal{D} , we optimize W^{out} by minimizing a squared error via continuous-time gradient descent (GD) to easily take the limit $N \rightarrow \infty$ [27–30].

We denote by $\theta_t \in \mathbb{R}^N$ and $f_t(x, \theta) \in \mathbb{R}$ the time-dependence of the vectorized output weights and $f_N(x)$ at time t , respectively. The dynamics of GD with the initialization $\theta_0 = \mathbf{0}$ yield the following formulae of the optimal output weights $(W^{\text{out}})^*$ and $f_N^*(x)$:

$$\begin{aligned} \theta_t &= \nabla_\theta f_0(\mathcal{X})^\top \hat{\Theta}_0^{-1} \left(I - e^{-\eta \hat{\Theta}_0 t} \right) \mathcal{Y}, \\ (W^{\text{out}})^{\ast\top} &= \lim_{t \rightarrow \infty} \theta_t = \nabla_\theta f_0(\mathcal{X})^\top \hat{\Theta}_0^{-1} \mathcal{Y}, \end{aligned} \quad (2)$$

$$\begin{aligned} f_t(x, \theta) &= \hat{\Theta}_0(x, \mathcal{X}) \hat{\Theta}_0^{-1} \left(I - e^{-\eta \hat{\Theta}_0 t} \right) \mathcal{Y}, \\ f_N^*(x) &= \lim_{t \rightarrow \infty} f_t(x, \theta) = \hat{\Theta}_0(x, \mathcal{X}) \hat{\Theta}_0^{-1} \mathcal{Y}, \end{aligned} \quad (3)$$

where $\eta > 0$ is a learning rate and $\nabla_\theta f_0(\mathcal{X}) \in \mathbb{R}^{|\mathcal{D}| \times N}$, $\hat{\Theta}_0(x, \mathcal{X}) \in \mathbb{R}^{1 \times |\mathcal{D}|}$, and $\hat{\Theta}_0 \in \mathbb{R}^{|\mathcal{D}| \times |\mathcal{D}|}$ are the matrices; these matrices are given in the following manner:

$$\begin{aligned} \nabla_\theta f_0(\mathcal{X})_{ij} &= \frac{1}{\sqrt{N}} \phi(h_j(x_i)), \quad \hat{\Theta}_0(x, \mathcal{X})_i \equiv \hat{\Theta}_0(x, x_i), \\ \hat{\Theta}_0 &\equiv \hat{\Theta}_0(\mathcal{X}, \mathcal{X}) \equiv \nabla_\theta f_0(\mathcal{X}) \nabla_\theta f_0(\mathcal{X})^\top, \end{aligned} \quad (4)$$

$$\hat{\Theta}_0(x, y) = \frac{1}{N} \sum_{i=1}^N \phi(h_i(x)) \phi(h_i(y)). \quad (5)$$

We note that $\hat{\Theta}_0$ is symmetric and assumed to be positive definite. Eqs. (2) and (4) yield

$$(W^{\text{out}})^{\ast\top} = \nabla_\theta f_0(\mathcal{X})^\top \left(\nabla_\theta f_0(\mathcal{X}) \nabla_\theta f_0(\mathcal{X})^\top \right)^{-1} \mathcal{Y},$$

implying that $\theta_0 = \mathbf{0}$ will lead W^{out} to the minimum norm solution (MNS) [29–32], which is given by the pseudoinverse of $\nabla_\theta f_0(\mathcal{X})$ (“extreme learning machine” [20, 21, 33]).

By the law of large numbers, $\hat{\Theta}_0(x, y)$ (Eq. (5)) converges in probability to $\Theta(x, y)$ —that is the expectation over random variables $[\omega, \beta] \sim \mathcal{N}(\mathbf{0}, \sigma^2 I)$ —in the limit $N \rightarrow \infty$ because the components of W^{in} and b^{in} follow

an iid Gaussian distribution [27]:

$$\Theta(x, y) = \frac{1}{2\pi\sigma^2} \int d\omega d\beta \phi(\omega x + \beta) \phi(\omega y + \beta) e^{-\frac{\omega^2 + \beta^2}{2\sigma^2}}. \quad (6)$$

$\Theta(x, y)$ is called the NTK [27]. Defining $\Theta(x, \mathcal{X})$ and Θ in the same manner as $\hat{\Theta}_0(x, y)$, we acquire $f_\infty^*(x)$, since $f_N^*(x)$ (Eq. (3)) is calculated from only the values of $\hat{\Theta}_0(x, y)$:

$$f_\infty^*(x) = \Theta(x, \mathcal{X}) \Theta^{-1} \mathcal{Y}, \quad (7)$$

where we again assume Θ to be positive definite. Moreover, the output of infinite-width ESN, which is described by recurrent kernels [34–36], reduces to the form of Eq. (7) in the limit where the regularization parameter goes to zero without considering the bias term of the network output.

With regard to learning period three, f_∞^* is given by

$$f_\infty^*(x) = \begin{bmatrix} \Theta(x, a) \\ \Theta(x, b) \\ \Theta(x, c) \end{bmatrix}^\top \begin{bmatrix} \Theta(a, a) & \Theta(a, b) & \Theta(a, c) \\ \Theta(b, a) & \Theta(b, b) & \Theta(b, c) \\ \Theta(c, a) & \Theta(c, b) & \Theta(c, c) \end{bmatrix}^{-1} \begin{bmatrix} b \\ c \\ a \end{bmatrix}. \quad (8)$$

To investigate the dynamics of f_∞^* , we compute the trajectory $\{x_n\}_{n=0}^T$ of $T+1 \gg 1$ steps with an initial state x_0 and calculate the Lyapunov exponent and period of attractors from trajectories. The Lyapunov exponent expresses the sensitivity of a dynamical system to initial conditions and is calculated using the following equation:

$$\lambda_T = \frac{1}{T} \sum_{n=1}^T \ln \left| \frac{d}{dx} f_\infty^*(x_n) \right|. \quad (9)$$

We regard a trajectory of f_∞^* as chaotic when $\lambda_T > 0$. Note that the derivative of f_∞^* is calculated by

$$\frac{d}{dx} f_\infty^*(x) = \frac{\partial}{\partial x} \Theta(x, \mathcal{X}) \Theta^{-1} \mathcal{Y}. \quad (10)$$

We also calculate the period of attractors as the minimum integer $n \in [1, n_{\max}]$ that satisfies the following inequality ($n_{\max} = 10$ or 20):

$$\frac{|(f_\infty^*)^n(x_T) - x_T|}{\max\{|x_T|, |(f_\infty^*)^n(x_T)|\}} \leq 10^{-12}, \quad (11)$$

where $(f_\infty^*)^1 \equiv f_\infty^*$, $(f_\infty^*)^{k+1} \equiv f_\infty^* \circ (f_\infty^*)^k$.

For $\phi = \text{erf}, \text{sin}, \text{cos}, \text{ReLU}$, there exist the analytical solutions of $\Theta(x, y)$ (Sec. IB in the Supplementary Material

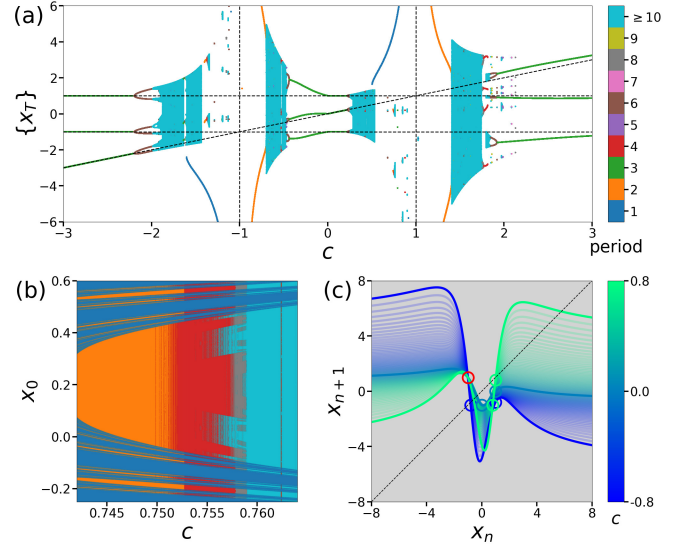


FIG. 2. Change in dynamical system f_∞^* for $\phi = \text{erf}$ with respect to c , with $a = -1$, $b = 1$, and $\sigma = 1.0$. The trajectory $\{x_n\}_{n=0}^T$ of $T = 10^5$ steps is computed with different x_0 and c in given intervals, excluding $c = a, b$. (a) Bifurcation diagram of the characteristic attractors calculated with $-10 \leq x_0 \leq 10$. The dotted lines indicate \mathcal{D} ; the diagonal line corresponds to a varying c . (b) Change in the basin of attraction where f_∞^* has multiple untrained attractors. (c) Change in the map f_∞^* in $-0.8 \leq c \leq 0.8$. The circles indicate \mathcal{D} and the red circle indicates a c -independent point $(a, b) = (-1, 1)$. As c approaches a or b , the folding of f_∞^* around \mathcal{D} becomes larger, making the characteristic attractors wider.

[23], which includes Refs. [37, 38]):

$$\begin{aligned} \Theta^{\text{erf}}(x, y) &= \frac{2}{\pi} \arcsin \frac{2\sigma^2(1+xy)}{\sqrt{[1+2\sigma^2(1+x^2)][1+2\sigma^2(1+y^2)]}}, \end{aligned} \quad (12)$$

$$\Theta^{\text{sin}}(x, y) = \frac{1}{2} \left\{ e^{-\frac{\sigma^2}{2}(x-y)^2} - e^{-\frac{\sigma^2}{2}(x+y)^2 - 2\sigma^2} \right\}, \quad (13)$$

$$\Theta^{\text{cos}}(x, y) = \frac{1}{2} \left\{ e^{-\frac{\sigma^2}{2}(x-y)^2} + e^{-\frac{\sigma^2}{2}(x+y)^2 - 2\sigma^2} \right\}, \quad (14)$$

$$\begin{aligned} \Theta^{\text{relu}}(x, y) &= \frac{\sigma^2}{2\pi} \sqrt{(1+x^2)(1+y^2)} \\ &\quad \left\{ \sqrt{1 - \cos^2 \psi} + (\pi - \psi) \cos \psi \right\}, \end{aligned} \quad (15)$$

where $\psi \equiv \arccos \frac{1+xy}{\sqrt{(1+x^2)(1+y^2)}}$. We note that the trajectories for a bounded activation function—such as $\phi = \text{erf}, \text{sin}, \text{cos}$ —are also bounded since $\Theta(x, y)$ (Eq. (6)) is the expectation of the product of ϕ . Moreover, as $\phi = \text{erf}, \text{sin}, \text{cos}$ and their corresponding NTKs are analytic, f_N^* and f_∞^* have finitely many attractors, according to Theorem B in Ref. [39] (Sec. II in the Supplementary Material [23], which includes Ref. [40]). In contrast, certain trajectories for $\phi = \text{ReLU}$, whose NTK is unbounded, will head toward infinity.

Figure 2 depicts how f_∞^* for $\phi = \text{erf}$ changes as c varies.

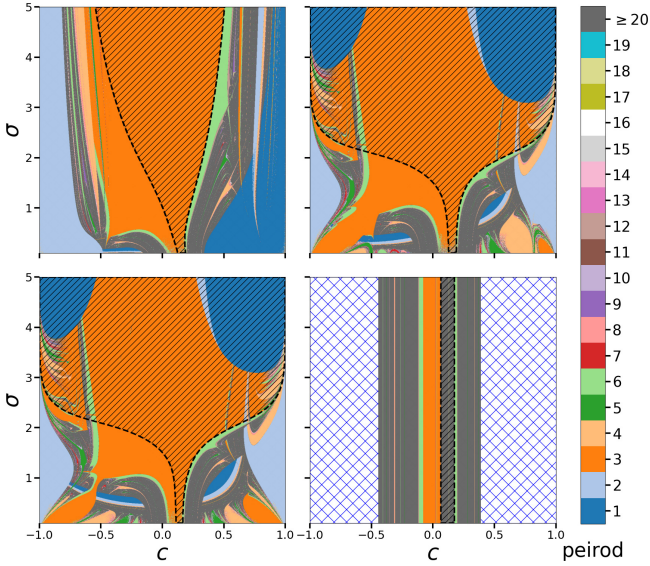


FIG. 3. Two-dimensional slices of the characteristic bifurcation structures for $\phi = \text{erf}$ (top left), \sin (top right), \cos (bottom left), and ReLU (bottom right) with respect to c and σ , with $a = -1$, $b = 1$, $x_0 = 0$, and $T = 10^4$. The black-hatched areas indicate the regions in which $|\frac{d}{dx} f_\infty^*(a) \frac{d}{dx} f_\infty^*(b) \frac{d}{dx} f_\infty^*(c)| < 1$ holds. They correspond to the regions of $\mathcal{D} = \{a, b, c\}$ being locally stable, implying that for $\phi = \text{erf}, \sin, \cos$, increasing σ stabilizes \mathcal{D} . The blue-hatched area in the bottom-right panel indicates the region (c, σ) , where the trajectory heads toward infinity.

Note that the trained network always includes \mathcal{D} since $f_N^*(\mathcal{X}) = f_\infty^*(\mathcal{X}) = \mathcal{Y}$. In the case of \mathcal{D} becoming the attractor ($-3 \leq c < -2.2$ and $0 < c \leq 0.22$), which corresponds to the successful attractor embedding by a learning machine, we observe that f_∞^* has no untrained attractors. However, varying c changes the stability of all the periods—including \mathcal{D} —together, resulting in the emergence of untrained attractors: untrained period-3 ($-0.43 \leq c < 0$ and $2 \leq c \leq 3$), chaotic ($c = -0.5, 0.3$, etc.), and multiple attractors ($0.742 \leq c \leq 0.764$, etc.). For $\phi = \sin, \cos, \text{ReLU}$, the bifurcation diagrams look very different from that in Fig. 2, but they have the same properties: only a handful of attractors appear at a time, which can be untrained ones (see Sec. IV in the Supplementary Material [23] for the bifurcation diagrams with the other network settings and the corresponding λ_T). We note that as the NTKs for $\phi = \text{erf}, \sin, \cos, \text{ReLU}$ depend on the scaling and translation of inputs, varying a or b , which we fixed, also yields a different bifurcation diagram. Nevertheless, the bifurcation structure has universal symmetry properties under the swapping of a and b (Sec. III in the Supplementary Material [23]). In particular, there is a qualitative correspondence between the outside ($c < a, b < c$) and the inside ($a < c < b$) bifurcation structure, if $b \approx -a$ (Fig. 2(a)).

As we expect from the above discussion, we observe

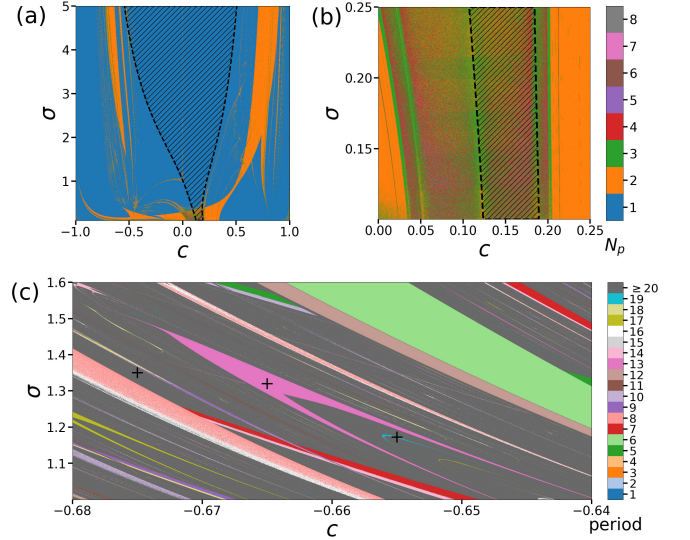


FIG. 4. Two-dimensional slices of the characteristic bifurcation structure for $\phi = \text{erf}$ with respect to c and σ , with $a = -1$, $b = 1$, and $T = 10^4$. (a) Number of kinds of period of attractors N_p calculated with 100 equidistant initial states in $-10 \leq x_0 \leq 10$. f_∞^* has roughly N_p attractors. (b) The zoom of (a). (c) The zoom of the top-left panel of Fig. 3. The black-hatched areas in (a),(b) indicate the regions of $\mathcal{D} = \{a, b, c\}$ being locally stable.

many types of characteristic attractors by varying σ along with \mathcal{D} (Figs. 3 and 4). Note that as f_∞^* may have multiple attractors (Fig. 4(a),(b)), certain trajectories reach attractors that are not depicted in Fig. 3. By utilizing these diagrams, we can control the untrained attractors of f_∞^* to obtain a large variety of attractors, which is extremely useful for generating intended dynamics. For example for $\phi = \text{erf}$, we obtain the period-13 attractor at $(c, \sigma) = (-0.665, 1.32)$, period-19 attractor at $(c, \sigma) = (-0.655, 1.172)$, and chaotic attractor at $(c, \sigma) = (-0.675, 1.35)$ (“+” in Fig. 4(c)). For $\phi = \text{ReLU}$, the σ -dependence of NTK (Eq.(15)) is canceled out, resulting in the uniform bifurcation structure along the σ -direction (the bottom-right panel of Fig. 3). In contrast, for $\phi = \text{erf}, \sin, \cos$, we can stabilize \mathcal{D} by increasing σ because the derivative of NTK at data point y approaches zero for large σ (the black-hatched areas in Fig. 3):

$$\begin{aligned} \frac{\partial}{\partial x} \Theta^{\text{erf}}(y, y) &= \frac{4\sigma^2 y}{\pi [1 + 2\sigma^2(1 + y^2)] \sqrt{1 + 4\sigma^2(1 + y^2)}}, \\ \frac{\partial}{\partial x} \Theta^{\sin}(y, y) &= -\frac{\partial}{\partial x} \Theta^{\cos}(y, y) = \sigma^2 y e^{-2\sigma^2(1 + y^2)}. \end{aligned}$$

However, $f_\infty^{*, \sin}$ and $f_\infty^{*, \cos}$ exponentially decrease to zero except at \mathcal{D} as σ grows; perturbations of x_0 from \mathcal{D} lead to their different attractors for large σ ; $\Theta^{\sin}(x, y)$ and $\Theta^{\cos}(x, y)$ become the Kronecker-delta-like functions in the infinite input-intensity limit $\sigma \rightarrow \infty$:

$$\lim_{\sigma \rightarrow \infty} \Theta^{\sin}(x, y) = \lim_{\sigma \rightarrow \infty} \Theta^{\cos}(x, y) = \frac{1}{2} \mathbf{1}_y(x), \quad (16)$$

where $\mathbf{1}_y(x) \equiv 1$ for $x = y$ and 0 otherwise. Interestingly, for $\phi = \text{erf}$, $\Theta^{\text{erf}}(x, y)$ and, therefore, $f_\infty^{*\text{erf}}$ becomes piecewise-monotonic and piecewise-smooth, with \mathcal{D} being its singular points in the limit $\sigma \rightarrow \infty$:

$$\lim_{\sigma \rightarrow \infty} \Theta^{\text{erf}}(x, y) = \frac{2}{\pi} \arcsin \frac{1 + xy}{\sqrt{(1 + x^2)(1 + y^2)}}, \quad (17)$$

$$\frac{\partial}{\partial x} \lim_{\sigma \rightarrow \infty} \Theta^{\text{erf}}(x, y) = \frac{-2}{\pi(1 + x^2)} \cdot \frac{x - y}{|x - y|}, \quad (18)$$

enabling the candidates of robust chaos [41, 42] to appear. In addition, in this limit, NTK for sigmoidal activation (17) is equivalent to that for binary activation ($\phi = \text{sgn}$) [36]. Although f_N^* for $\phi = \text{sgn}$ is beyond the scope of theorems 1 and 2, it asymptotically approaches a continuous map f_∞^* , exhibiting multiple stable periodic orbits for large N . Finite-size effects also emerge for $\phi = \sin, \cos$, which are caused by the wavy deviations of f_N^* from f_∞^* (Sec. IV in the Supplementary Material [23]).

Finally, we discuss the peculiarity of learning period three with MNS and the scalability of our thermodynamic limit analysis in dynamical systems learning. Since $f_\infty^*(x)$ is described by the multiplication of $\Theta(x, \mathcal{X})$ and Θ^{-1} , $|\mathcal{D}|$ crucially affects the complexity of the theoretical analysis of f_∞^* . Accordingly, the longer the target orbit becomes—such as in the case of learning chaos and learning continuous-time dynamical systems from time series—the fewer the benefits of our proposed approach. However, similar to learning period three, if we adopt the strategy of exploiting the intrinsic mathematical structure of a learning machine with a small amount of training data, infinite-width networks provide a novel perspective to dynamical systems learning. We also investigated how the learned periods depend on the target period number n and found that regardless of the choice of ϕ , the number of unstable periods tends to increase dramatically after $n = 3$ (Sec. V in the Supplementary Material [23]). This result suggests that a rich characteristic bifurcation structure is obtained by a combination of bulk unstable periods ensured by learning period three and a change in their stability through the system’s nonlinearity, which is our answer to the very first question.

As an engineering application, our results suggest that various types of dynamics, including higher-order periodic orbits and chaos, can be obtained by teaching only three target data points to the network with appropriate settings. More importantly, the network may be a physical system or neuromorphic device, such as the physical reservoir computer [43]; embedding desirable dynamics into physical systems would be highly beneficial, for example, in a high-radiation environment in which a computer-simulated attractor may break down [44]. We leave the thermodynamic limit analysis of a physical neural network for future work.

We are grateful to Allen Hart for the fruitful discus-

sions on attractor embedding in RC and to the RC seminar members for the stimulating discussions.

* terasaki@isi.imi.i.u-tokyo.ac.jp

† k-nakajima@isi.imi.i.u-tokyo.ac.jp

- [1] K. Nakajima and I. Fischer, *Reservoir Computing* (Springer, Singapore, 2021).
- [2] H. Jaeger, The “echo state” approach to analysing and training recurrent neural networks-with an erratum note, Bonn, Germany: German National Research Center for Information Technology GMD Technical Report **148**, 13 (2001).
- [3] J. Pathak, Z. Lu, B. R. Hunt, M. Girvan, and E. Ott, Using machine learning to replicate chaotic attractors and calculate Lyapunov exponents from data, *Chaos: An Interdisciplinary Journal of Nonlinear Science* **27**, 121102 (2017).
- [4] Z. Lu, B. R. Hunt, and E. Ott, Attractor reconstruction by machine learning, *Chaos: An Interdisciplinary Journal of Nonlinear Science* **28**, 061104 (2018).
- [5] A. Hart, J. Hook, and J. Dawes, Embedding and approximation theorems for echo state networks, *Neural Networks* **128**, 234 (2020).
- [6] L. Grigoryeva, A. Hart, and J.-P. Ortega, Chaos on compact manifolds: Differentiable synchronizations beyond the takens theorem, *Phys. Rev. E* **103**, 062204 (2021).
- [7] L. Grigoryeva, A. Hart, and J.-P. Ortega, Learning strange attractors with reservoir systems, *Nonlinearity* **36**, 4674 (2023).
- [8] A. Flynn, V. A. Tsachouridis, and A. Amann, Multifunctionality in a reservoir computer, *Chaos: An Interdisciplinary Journal of Nonlinear Science* **31**, 013125 (2021).
- [9] A. Flynn, V. A. Tsachouridis, and A. Amann, Seeing double with a multifunctional reservoir computer, *Chaos: An Interdisciplinary Journal of Nonlinear Science* **33**, 113115 (2023).
- [10] J. Z. Kim, Z. Lu, E. Nozari, G. J. Pappas, and D. S. Bassett, Teaching recurrent neural networks to infer global temporal structure from local examples, *Nature Machine Intelligence* **3**, 316 (2021).
- [11] H. Fan, L. Wang, Y. Du, Y. Wang, J. Xiao, and X. Wang, Learning the dynamics of coupled oscillators from transients, *Phys. Rev. Res.* **4**, 013137 (2022).
- [12] A. Röhm, D. J. Gauthier, and I. Fischer, Model-free inference of unseen attractors: Reconstructing phase space features from a single noisy trajectory using reservoir computing, *Chaos: An Interdisciplinary Journal of Nonlinear Science* **31**, 103127 (2021).
- [13] S. Steingrube, M. Timme, F. Wörgötter, and P. Manoonpong, Self-organized adaptation of a simple neural circuit enables complex robot behaviour, *Nature physics* **6**, 224 (2010).
- [14] A. J. Ijspeert, A. Crespi, D. Ryczko, and J.-M. Cabelguen, From swimming to walking with a salamander robot driven by a spinal cord model, *Science* **315**, 1416 (2007).
- [15] N. Akashi, Y. Kuniyoshi, T. Jo, M. Nishida, R. Sakurai, Y. Wakao, and K. Nakajima, Embedding bifurcations into pneumatic artificial muscle, *Advanced Science* **n/a**, 2304402 (2024).

- [16] K. Burns and B. Hasselblatt, The sharkovsky theorem: A natural direct proof, *The American Mathematical Monthly* **118**, 229 (2011).
- [17] A. M. Blokh and O. M. Sharkovsky, *Sharkovsky Ordering* (Springer, Cham, 2022).
- [18] T.-Y. Li and J. A. Yorke, Period three implies chaos, *The American Mathematical Monthly* **82**, 985 (1975).
- [19] R. Tokunaga, S. Kajiwara, and T. Matsumoto, Reconstructing bifurcation diagrams only from time-waveforms, *Physica D: Nonlinear Phenomena* **79**, 348 (1994).
- [20] Y. Itoh, Y. Tada, and M. Adachi, Reconstructing bifurcation diagrams with lyapunov exponents from only time-series data using an extreme learning machine, *Nonlinear Theory and Its Applications, IEICE* **8**, 2 (2017).
- [21] Y. Itoh, S. Uenohara, M. Adachi, T. Morie, and K. Aihara, Reconstructing bifurcation diagrams only from time-series data generated by electronic circuits in discrete-time dynamical systems, *Chaos: An Interdisciplinary Journal of Nonlinear Science* **30**, 013128 (2020).
- [22] M. Hara and H. Kokubu, Learning dynamics by reservoir computing (in memory of prof. pavol brunovský), *Journal of Dynamics and Differential Equations* **36**, 515 (2024).
- [23] See Supplementary Material for the other network settings, detailed derivation of the thermodynamic limit, the analytic solutions for NTK, GD with ridge regularization, the finiteness of the attractors for the bounded analytic NTK, the symmetries in learning period three, the characteristic bifurcation structures with the other network settings, the corresponding Lyapunov exponents, the finite-size effects in learning period three, and learning period $n = 1, 2, 3, \dots$, which include Refs. [24–26, 37, 38, 40].
- [24] M. Sahræe-Ardakan, M. Emami, P. Pandit, S. Rangan, and A. K. Fletcher, Kernel methods and multi-layer perceptrons learn linear models in high dimensions (2022), arXiv:2201.08082 [stat.ML].
- [25] C. Saunders, A. Gammernan, and V. Vovk, Ridge regression learning algorithm in dual variables, in *Proceedings of the 15th International Conference on Machine Learning, ICML'98* (Morgan Kaufmann, San Francisco, CA, 1998) pp. 515–521.
- [26] J. Suykens, Nonlinear modelling and support vector machines, in *IMTC 2001. Proceedings of the 18th IEEE Instrumentation and Measurement Technology Conference. Rediscovering Measurement in the Age of Informatics (Cat. No.01CH 37188)*, Vol. 1 (2001) pp. 287–294 vol.1.
- [27] A. Jacot, F. Gabriel, and C. Hongler, Neural tangent kernel: Convergence and generalization in neural networks, in *Advances in Neural Information Processing Systems*, Vol. 31, edited by S. Bengio, H. Wallach, H. Larochelle, K. Grauman, N. Cesa-Bianchi, and R. Garnett (Curran Associates, Inc., 2018).
- [28] J. Lee, L. Xiao, S. Schoenholz, Y. Bahri, R. Novak, J. Sohl-Dickstein, and J. Pennington, Wide neural networks of any depth evolve as linear models under gradient descent, in *Advances in Neural Information Processing Systems*, Vol. 32, edited by H. Wallach, H. Larochelle, A. Beygelzimer, F. d'Alché-Buc, E. Fox, and R. Garnett (Curran Associates, Inc., 2019).
- [29] A. Ali, J. Z. Kolter, and R. J. Tibshirani, A continuous-time view of early stopping for least squares regression, in *Proceedings of the Twenty-Second International Conference on Artificial Intelligence and Statistics*, Proceedings of Machine Learning Research, Vol. 89, edited by K. Chaudhuri and M. Sugiyama (PMLR, 2019) pp. 1370–1378.
- [30] M. S. Advani, A. M. Saxe, and H. Sompolinsky, High-dimensional dynamics of generalization error in neural networks, *Neural Networks* **132**, 428 (2020).
- [31] T. Liang and A. Rakhlin, Just interpolate: Kernel “ridgeless” regression can generalize, *The Annals of Statistics* **48**, 1329 (2020).
- [32] T. Hastie, A. Montanari, S. Rosset, and R. J. Tibshirani, Surprises in high-dimensional ridgeless least squares interpolation, *The Annals of Statistics* **50**, 949 (2022).
- [33] G.-B. Huang, Q.-Y. Zhu, and C.-K. Siew, Extreme learning machine: Theory and applications, *Neurocomputing* **70**, 489 (2006), neural Networks.
- [34] M. Hermans and B. Schrauwen, Recurrent kernel machines: Computing with infinite echo state networks, *Neural Computation* **24**, 104 (2012).
- [35] J. Dong, R. Ohana, M. Rafayelyan, and F. Krzakala, Reservoir computing meets recurrent kernels and structured transforms, in *Advances in Neural Information Processing Systems*, Vol. 33, edited by H. Larochelle, M. Ranzato, R. Hadsell, M. Balcan, and H. Lin (Curran Associates, Inc., 2020) pp. 16785–16796.
- [36] J. Dong, E. Börve, M. Rafayelyan, and M. Unser, Asymptotic stability in reservoir computing, in *2022 International Joint Conference on Neural Networks (IJCNN)* (2022) pp. 01–08.
- [37] C. Williams, Computing with infinite networks, in *Advances in Neural Information Processing Systems*, Vol. 9, edited by M. Mozer, M. Jordan, and T. Petsche (MIT Press, 1996).
- [38] Y. Cho and L. Saul, Kernel methods for deep learning, in *Advances in Neural Information Processing Systems*, Vol. 22, edited by Y. Bengio, D. Schuurmans, J. Lafferty, C. Williams, and A. Culotta (Curran Associates, Inc., 2009).
- [39] W. De Melo and S. Van Strien, *One-Dimensional Dynamics* (Springer, Berlin, 1993).
- [40] S. v. Strien, T. Bedford, and H. Swift, Smooth dynamics on the interval (with an emphasis on quadratic-like maps), in *New Directions in Dynamical Systems*, London Mathematical Society Lecture Note Series (Cambridge University Press, 1988) p. 57–119.
- [41] S. Banerjee, J. A. Yorke, and C. Grebogi, Robust chaos, *Phys. Rev. Lett.* **80**, 3049 (1998).
- [42] S. Banerjee, M. Karthik, G. Yuan, and J. Yorke, Bifurcations in one-dimensional piecewise smooth maps-theory and applications in switching circuits, *IEEE Transactions on Circuits and Systems I: Fundamental Theory and Applications* **47**, 389 (2000).
- [43] K. Nakajima, Physical reservoir computing—an introductory perspective, *Japanese Journal of Applied Physics* **59**, 060501 (2020).
- [44] N. Akashi, Y. Kuniyoshi, S. Tsunegi, T. Taniguchi, M. Nishida, R. Sakurai, Y. Wakao, K. Kawashima, and K. Nakajima, A coupled spintronics neuromorphic approach for high-performance reservoir computing, *Advanced Intelligent Systems* **4**, 2200123 (2022).

Supplementary Material for “Thermodynamic Limit in Learning Period Three”

Yuichiro Terasaki^{1,*} and Kohei Nakajima^{2,3,†}

¹*Department of Mechano-Informatics, The University of Tokyo, Tokyo 113-8656, Japan*

²*Graduate School of Information Science and Technology,
The University of Tokyo, Tokyo 113-8656, Japan*

³*Next Generation Artificial Intelligence Research Center,
The University of Tokyo, Tokyo 113-8656, Japan*

(Dated: May 11, 2024)

This supplementary material describes the derivation procedures, calculations, numerical experiments, and additional figures in detail. We assign the numbers of equations, figures, and propositions here with S and specify the equations and figures by the same numbers in the main text.

CONTENTS

I. Thermodynamic Limit of the Learning Machine	8
A. Derivation of the Trained Network Output	8
B. Analytic Solutions for Neural Tangent Kernels	10
C. Networks with Uniform Distributions	12
D. Learning with Ridge Regularization	12
II. Finiteness of the Attractors of the Trained Map with the Bounded Analytic NTK	14
III. Symmetries in Learning Period Three	14
IV. Learning Machine Dynamics for $\phi = \text{erf}, \sin, \cos, \text{ReLU}$	18
V. Learning Period $n = 1, 2, 3, \dots$	23
References	25

* terasaki@isi.imi.i.u-tokyo.ac.jp

† k-nakajima@isi.imi.i.u-tokyo.ac.jp

I. THERMODYNAMIC LIMIT OF THE LEARNING MACHINE

A. Derivation of the Trained Network Output

Here, we define the neural network output $f_N(x)$ for an input $x \in \mathbb{R}$ as follows:

$$\begin{aligned} h_i(x) &\equiv W_i^{\text{in}}x + b_i^{\text{in}} \quad (i = 1, \dots, N) \\ f_N(x) &\equiv \frac{1}{\sqrt{N}} \sum_{i=1}^N W_i^{\text{out}} \phi(h_i(x)), \quad f_N^{\text{bias}}(x) \equiv \frac{1}{\sqrt{N}} \sum_{i=1}^N W_i^{\text{out}} \phi(h_i(x)) + b^{\text{out}} \\ W_i^{\text{in}} &\sim \mathcal{N}(0, \sigma_w^2), \quad b_i^{\text{in}} \sim \mathcal{N}(0, \sigma_b^2), \end{aligned} \quad (\text{S1})$$

where $W^{\text{in}} \in \mathbb{R}^{N \times 1}$ and $b^{\text{in}} \in \mathbb{R}^N$ are the input weights and biases randomly drawn from Gaussian distributions, respectively, $\phi: \mathbb{R} \rightarrow \mathbb{R}$ is an activation function, and $W^{\text{out}} \in \mathbb{R}^{1 \times N}$ and $b^{\text{out}} \in \mathbb{R}$ are the output weights and bias optimized by a learning method described below, respectively. We can reduce this network model to that in the main text by assuming $\sigma_w = \sigma_b = \sigma$ without b^{out} . As outlined in the main text, we consider specific activation functions $\phi = \text{erf}, \sin, \cos, \text{ReLU}$ and use the same notations for the target input–output pairs: \mathcal{D} , $|\mathcal{D}|$, \mathcal{X} , and \mathcal{Y} .

For a given \mathcal{D} , we assume sufficiently many nodes $N \geq |\mathcal{D}|$ and consider the virtual learning dynamics of W^{out} (and b^{out}) using continuous-time gradient descent (GD) [1–4]. We denote the time dependence of the vectorized output parameters by $\theta_t \equiv [\theta_1(t), \dots, \theta_{N_\theta}(t)] \in \mathbb{R}^{N_\theta}$:

$$\begin{aligned} \theta_t &= [W_1^{\text{out}}(t), \dots, W_N^{\text{out}}(t)], \quad N_\theta = N \\ \theta_t^{\text{bias}} &= [W_1^{\text{out}}(t), \dots, W_N^{\text{out}}(t), b^{\text{out}}(t)], \quad N_\theta^{\text{bias}} = N + 1. \end{aligned} \quad (\text{S2})$$

We also denote the time dependence of the neural network output by $f_t(x, \theta) \in \mathbb{R}$, optimize the output parameters by minimizing the squared error (SE)

$$\mathcal{L} = \frac{1}{2} \sum_{(x_i, y_i) \in \mathcal{D}} \{f_t(x_i, \theta) - y_i\}^2 = \frac{1}{2} \|f_t(\mathcal{X}) - \mathcal{Y}\|^2 \quad \text{where} \quad f_t(\mathcal{X}) \equiv [f_t(x_1, \theta), \dots, f_t(x_{|\mathcal{D}|}, \theta)] \in \mathbb{R}^{|\mathcal{D}|}, \quad (\text{S3})$$

and consider the following ordinary differential equation (ODE) of θ_t :

$$\dot{\theta}_t = -\eta \nabla_\theta \mathcal{L} = -\eta \nabla_\theta f_t(\mathcal{X})^\top \nabla_{f_t(\mathcal{X})} \mathcal{L} \quad \text{where} \quad \nabla_\theta f_t(\mathcal{X}) \equiv \begin{bmatrix} \frac{\partial}{\partial \theta_1} f_t(x_1, \theta) & \cdots & \frac{\partial}{\partial \theta_{N_\theta}} f_t(x_1, \theta) \\ \vdots & \ddots & \vdots \\ \frac{\partial}{\partial \theta_1} f_t(x_{|\mathcal{D}|}, \theta) & \cdots & \frac{\partial}{\partial \theta_{N_\theta}} f_t(x_{|\mathcal{D}|}, \theta) \end{bmatrix} \in \mathbb{R}^{|\mathcal{D}| \times N_\theta}. \quad (\text{S4})$$

Here, η is a learning rate, which may be any value greater than 0. We note that the optimized parameters θ^* are given by the limit $t \rightarrow \infty$ of the solution θ_t of Eq.(S4). Applying $\nabla_{f_t(\mathcal{X})} \mathcal{L} = f_t(\mathcal{X}) - \mathcal{Y}$ to Eq. (S4) and combining Eq. (S4) with $\dot{f}_t(\mathcal{X}) = \nabla_\theta f_t(\mathcal{X}) \dot{\theta}_t$ (the chain rule), we get:

$$\dot{\theta}_t = -\eta \nabla_\theta f_t(\mathcal{X})^\top (f_t(\mathcal{X}) - \mathcal{Y}) \quad (\text{S5})$$

$$\dot{f}_t(\mathcal{X}) = -\eta \hat{\Theta}_t(\mathcal{X}, \mathcal{X}) (f_t(\mathcal{X}) - \mathcal{Y}) \quad \text{where} \quad \hat{\Theta}_t(\mathcal{X}, \mathcal{X}) \equiv \nabla_\theta f_t(\mathcal{X}) \nabla_\theta f_t(\mathcal{X})^\top \in \mathbb{R}^{|\mathcal{D}| \times |\mathcal{D}|}. \quad (\text{S6})$$

Here, $\hat{\Theta}_t(\mathcal{X}, \mathcal{X})$ is the Gram matrix whose size is $|\mathcal{D}| \times |\mathcal{D}|$. Generalizing this matrix to any input $x, y \in \mathbb{R}$, we define the following kernel $\hat{\Theta}_t(\cdot, \cdot): \mathbb{R} \times \mathbb{R} \rightarrow \mathbb{R}$:

$$\hat{\Theta}_t(x, y) \equiv \nabla_\theta f_t(x, \theta) \nabla_\theta f_t(y, \theta)^\top \quad (x, y \in \mathbb{R}) \quad \text{where} \quad \nabla_\theta f_t(x, \theta) \equiv \left[\frac{\partial}{\partial \theta_1} f_t(x, \theta) \quad \cdots \quad \frac{\partial}{\partial \theta_{N_\theta}} f_t(x, \theta) \right] \in \mathbb{R}^{1 \times N_\theta}. \quad (\text{S7})$$

Applying our network model (Eq. (S1)) to this definition, we get

$$\hat{\Theta}_t(x, y) = \frac{1}{N} \sum_{i=1}^N \phi(W_i^{\text{in}}x + b_i^{\text{in}}) \phi(W_i^{\text{in}}y + b_i^{\text{in}}), \quad \hat{\Theta}_t^{\text{bias}}(x, y) = \frac{1}{N} \sum_{i=1}^N \phi(W_i^{\text{in}}x + b_i^{\text{in}}) \phi(W_i^{\text{in}}y + b_i^{\text{in}}) + 1. \quad (\text{S8})$$

As $\hat{\Theta}_t(x, y)$ and $\hat{\Theta}_t^{\text{bias}}(x, y)$ in Eq. (S8) do not depend on t , we have $\hat{\Theta}_t(\mathcal{X}, \mathcal{X}) = \hat{\Theta}_0(\mathcal{X}, \mathcal{X})$ and $\hat{\Theta}_t^{\text{bias}}(\mathcal{X}, \mathcal{X}) = \hat{\Theta}_0^{\text{bias}}(\mathcal{X}, \mathcal{X})$ for any $t > 0$. Thus, we obtain the following solution of Eq. (S6):

$$f_t(\mathcal{X}) = \left(I - e^{-\eta \hat{\Theta}_0 t} \right) \mathcal{Y} + e^{-\eta \hat{\Theta}_0 t} f_0(\mathcal{X}) \quad (\text{S9})$$

where we write $\hat{\Theta}_0 \equiv \hat{\Theta}_0(\mathcal{X}, \mathcal{X})$ for the sake of simplicity. Assuming $\hat{\Theta}_0$ to be positive definite, the trained network always replicates the target input–output pairs as $e^{-\eta\hat{\Theta}_0 t} \rightarrow 0$ ($t \rightarrow \infty$), regardless of the initial values of the output parameters θ_0 :

$$f_N^*(\mathcal{X}) = \lim_{t \rightarrow \infty} f_t(\mathcal{X}) = \mathcal{Y}. \quad (\text{S10})$$

Substituting Eq. (S9) into Eq. (S5), we can obtain the solution θ_t for Eq. (S5):

$$\dot{\theta}_t = -\eta \nabla_{\theta} f_t(\mathcal{X})^{\top} e^{-\eta\hat{\Theta}_0 t} (f_0(\mathcal{X}) - \mathcal{Y}), \quad \theta_t = \nabla_{\theta} f_0(\mathcal{X})^{\top} \hat{\Theta}_0^{-1} \left(e^{-\eta\hat{\Theta}_0 t} - I \right) (f_0(\mathcal{X}) - \mathcal{Y}) + \theta_0. \quad (\text{S11})$$

Further, as the network output $f_t(x, \theta)$ is linear with respect to θ_t , we get

$$\begin{aligned} f_t(x, \theta) &= \nabla_{\theta} f_t(x, \theta) \theta_t = \nabla_{\theta} f_0(x, \theta) \theta_t \\ &= \nabla_{\theta} f_0(x, \theta) \nabla_{\theta} f_0(\mathcal{X})^{\top} \hat{\Theta}_0^{-1} \left(e^{-\eta\hat{\Theta}_0 t} - I \right) (f_0(\mathcal{X}) - \mathcal{Y}) + \nabla_{\theta} f_0(x, \theta) \theta_0 \\ &= \hat{\Theta}_0(x, \mathcal{X}) \hat{\Theta}_0^{-1} \left(e^{-\eta\hat{\Theta}_0 t} - I \right) (f_0(\mathcal{X}) - \mathcal{Y}) + f_0(x, \theta) \end{aligned} \quad (\text{S12})$$

$$\text{where } \hat{\Theta}_0(x, \mathcal{X}) \equiv \nabla_{\theta} f_0(x, \theta) \nabla_{\theta} f_0(\mathcal{X})^{\top} = [\hat{\Theta}_0(x, x_1) \ \cdots \ \hat{\Theta}_0(x, x_{|\mathcal{D}|})] \in \mathbb{R}^{1 \times |\mathcal{D}|}.$$

Therefore, the optimized parameters θ^* and the trained network output $f_N^*(x)$ are given by

$$\theta^* \equiv \lim_{t \rightarrow \infty} \theta_t = \nabla_{\theta} f_0(\mathcal{X})^{\top} \hat{\Theta}_0^{-1} (\mathcal{Y} - f_0(\mathcal{X})) + \theta_0 \quad (\text{S13})$$

$$f_N^*(x) \equiv \lim_{t \rightarrow \infty} f_t(x, \theta) = \hat{\Theta}_0(x, \mathcal{X}) \hat{\Theta}_0^{-1} (\mathcal{Y} - f_0(\mathcal{X})) + f_0(x, \theta). \quad (\text{S14})$$

We note that θ_0 remains as hyperparameters of θ^* and $f_N^*(x)$. This property corresponds to that if $N > |\mathcal{D}|$, minimizing the SE is underdetermined, and infinitely many candidates for θ^* exist. Now, by considering the case $\theta_0 = \mathbf{0}$ and using the the linearity of $f_t(x, \theta)$, we obtain $f_0(\mathcal{X}) = \mathbf{0}$, $f_0(x, \theta) = 0$ and

$$\theta^*|_{\theta_0=\mathbf{0}} = \nabla_{\theta} f_0(\mathcal{X})^{\top} \hat{\Theta}_0^{-1} \mathcal{Y} = \nabla_{\theta} f_0(\mathcal{X})^{\top} (\nabla_{\theta} f_0(\mathcal{X}) \nabla_{\theta} f_0(\mathcal{X})^{\top})^{-1} \mathcal{Y} \quad (\text{S15})$$

$$f_N^*(x)|_{\theta_0=\mathbf{0}} = \hat{\Theta}_0(x, \mathcal{X}) \hat{\Theta}_0^{-1} \mathcal{Y}, \quad (\text{S16})$$

meaning that $\theta_0 = \mathbf{0}$ will lead θ_t to the minimum norm solution (MNS) given by the pseudoinverse of the matrix $\nabla_{\theta} f_0(\mathcal{X})$ [3–6]. Since $f_N^*(x)$ (Eq. (S16)) is calculated from only the values of the kernel $\hat{\Theta}_0(x, y)$ (Eq. (S8)), we acquire the thermodynamic limit $f_{\infty}^*(x)$ from the limit $N \rightarrow \infty$ of $\hat{\Theta}_0(x, y)$. In this limit, $\hat{\Theta}_0(x, y)$ converges in probability to the neural tangent kernel (NTK) $\Theta(x, y)$ —that is the expectation over random variables $[\omega, \beta] \sim \mathcal{N}(\mathbf{0}, \text{diag}(\sigma_w^2, \sigma_b^2))$ —by the law of large numbers [1]:

$$\begin{aligned} \hat{\Theta}_0(x, y) &\rightarrow \Theta(x, y) = \mathbb{E} [\phi(\omega x + \beta) \phi(\omega y + \beta)] = \frac{1}{2\pi\sigma_w\sigma_b} \int d\omega d\beta \phi(\omega x + \beta) \phi(\omega y + \beta) e^{-\frac{1}{2} \left(\frac{\omega^2}{\sigma_w^2} + \frac{\beta^2}{\sigma_b^2} \right)} \\ \hat{\Theta}_0^{\text{bias}}(x, y) &\rightarrow \Theta^{\text{bias}}(x, y) = \Theta(x, y) + 1. \end{aligned} \quad (\text{S17})$$

Eqs. (S8) and (S17) indicate that if $\hat{\Theta}_0$ and Θ are positive definite, then $\hat{\Theta}_0^{\text{bias}}$ and Θ^{bias} are also positive definite; however, we note that the existence of b^{out} does not ensure the positive definiteness of $\hat{\Theta}_0$ or Θ . Defining the matrices $\Theta(x, \mathcal{X})$ and Θ in the same manner as $\hat{\Theta}_0(x, y)$, we obtain $f_{\infty}^*(x)$ as the weighted sum of NTK:

$$f_{\infty}^*(x) = \Theta(x, \mathcal{X}) \Theta^{-1} \mathcal{Y} = [\Theta(x, x_1) \ \cdots \ \Theta(x, x_{|\mathcal{D}|})] \begin{bmatrix} \Theta(x_1, x_1) & \cdots & \Theta(x_1, x_{|\mathcal{D}|}) \\ \vdots & \ddots & \vdots \\ \Theta(x_{|\mathcal{D}|}, x_1) & \cdots & \Theta(x_{|\mathcal{D}|}, x_{|\mathcal{D}|}) \end{bmatrix}^{-1} \begin{bmatrix} y_1 \\ \vdots \\ y_{|\mathcal{D}|} \end{bmatrix}, \quad (\text{S18})$$

where we again assume the matrix Θ to be positive definite. Similarly, the derivative of f_{∞}^* is given by the weighted sum of the partial derivatives of NTK:

$$\frac{d}{dx} f_{\infty}^*(x) = \frac{\partial}{\partial x} \Theta(x, \mathcal{X}) \Theta^{-1} \mathcal{Y} = \left[\frac{\partial}{\partial x} \Theta(x, x_1) \ \cdots \ \frac{\partial}{\partial x} \Theta(x, x_{|\mathcal{D}|}) \right] \begin{bmatrix} \Theta(x_1, x_1) & \cdots & \Theta(x_1, x_{|\mathcal{D}|}) \\ \vdots & \ddots & \vdots \\ \Theta(x_{|\mathcal{D}|}, x_1) & \cdots & \Theta(x_{|\mathcal{D}|}, x_{|\mathcal{D}|}) \end{bmatrix}^{-1} \begin{bmatrix} y_1 \\ \vdots \\ y_{|\mathcal{D}|} \end{bmatrix}. \quad (\text{S19})$$

B. Analytic Solutions for Neural Tangent Kernels

In this subsection, we provide the analytical solutions of $\Theta(x, y)$ for the activation functions $\phi = \text{erf}, \sin, \cos, \text{ReLU}$. Following Williams [7], the NTK for $\phi = \text{erf}$ is given by

$$\Theta^{\text{erf}}(x, y) = \frac{2}{\pi} \arcsin \frac{2(\sigma_b^2 + \sigma_w^2 xy)}{\sqrt{[1 + 2(\sigma_b^2 + \sigma_w^2 x^2)][1 + 2(\sigma_b^2 + \sigma_w^2 y^2)]}}. \quad (\text{S20})$$

Following Cho and Saul [8], the NTK for $\phi = \text{ReLU}$ is given by

$$\Theta^{\text{relu}}(x, y) = \frac{1}{2\pi} \sqrt{(\sigma_b^2 + \sigma_w^2 x^2)(\sigma_b^2 + \sigma_w^2 y^2)} \left\{ \sqrt{1 - \frac{(\sigma_b^2 + \sigma_w^2 xy)^2}{(\sigma_b^2 + \sigma_w^2 x^2)(\sigma_b^2 + \sigma_w^2 y^2)}} + (\pi - \psi) \frac{\sigma_b^2 + \sigma_w^2 xy}{\sqrt{(\sigma_b^2 + \sigma_w^2 x^2)(\sigma_b^2 + \sigma_w^2 y^2)}} \right\}$$

where $\psi \equiv \arccos \frac{\sigma_b^2 + \sigma_w^2 xy}{\sqrt{(\sigma_b^2 + \sigma_w^2 x^2)(\sigma_b^2 + \sigma_w^2 y^2)}}.$

(S21)

Here, $0 \leq \psi \leq \pi$ is an angle between the vectors $[\sigma_b, \sigma_w x], [\sigma_b, \sigma_w y] \in \mathbb{R}^2$, indicating the similarity between x and y . In the following, we derive NTKs for $\phi = \sin, \cos$. By using the formulae $\sin(\omega x + \beta) \sin(\omega y + \beta) = \{\cos[\omega(x - y)] - \cos[\omega(x + y) + 2\beta]\}/2$ and $\cos(\omega x + \beta) \cos(\omega y + \beta) = \{\cos[\omega(x - y)] + \cos[\omega(x + y) + 2\beta]\}/2$, we get

$$\Theta^{\sin}(x, y) = I_1 - I_2, \quad \Theta^{\cos}(x, y) = I_1 + I_2,$$

$$\text{where } I_1 \equiv \frac{1}{4\pi\sigma_w\sigma_b} \int d\omega d\beta \cos[\omega(x - y)] e^{-\frac{1}{2}\left(\frac{\omega^2}{\sigma_w^2} + \frac{\beta^2}{\sigma_b^2}\right)} \text{ and } I_2 \equiv \frac{1}{4\pi\sigma_w\sigma_b} \int d\omega d\beta \cos[\omega(x + y) + 2\beta] e^{-\frac{1}{2}\left(\frac{\omega^2}{\sigma_w^2} + \frac{\beta^2}{\sigma_b^2}\right)}. \quad (\text{S22})$$

Applying the Gaussian integral formula to I_1 and I_2 in Eq. (S22), we get

$$I_1 = \frac{1}{4\pi\sigma_w\sigma_b} \int_{-\infty}^{\infty} d\beta e^{-\frac{\beta^2}{2\sigma_b^2}} \int_{-\infty}^{\infty} d\omega \cos[\omega(x - y)] e^{-\frac{\omega^2}{2\sigma_w^2}} \quad (\text{S23})$$

$$= \frac{1}{2\sqrt{2\pi}\sigma_w} \int_{-\infty}^{\infty} d\omega \cos[\omega(x - y)] e^{-\frac{\omega^2}{2\sigma_w^2}} = \frac{1}{2\sqrt{2\pi}\sigma_w} \text{Re} \left[\int_{-\infty}^{\infty} d\omega e^{-\frac{\omega^2}{2\sigma_w^2} + i\omega(x - y)} \right] = \frac{e^{-\frac{\sigma_w^2}{2}(x - y)^2}}{2}$$

$$I_2 = \frac{1}{2} \text{Re} \left[\frac{1}{\sqrt{2\pi}\sigma_b} \int_{-\infty}^{\infty} d\beta e^{-\frac{\beta^2}{2\sigma_b^2} + 2i\beta} \frac{1}{\sqrt{2\pi}\sigma_w} \int_{-\infty}^{\infty} d\omega e^{-\frac{\omega^2}{2\sigma_w^2} + i\omega(x + y)} \right] = \frac{e^{-\frac{\sigma_w^2}{2}(x + y)^2 - 2\sigma_b^2}}{2}. \quad (\text{S24})$$

Here, Re is the real-part operator. Substituting Eqs. (S23)–(S24) into Eq. (S22), we obtain the following formulae of the NTKs for $\phi = \sin, \cos$:

$$\Theta^{\sin}(x, y) = \frac{1}{2} \left\{ e^{-\frac{\sigma_w^2}{2}(x - y)^2} - e^{-\frac{\sigma_w^2}{2}(x + y)^2 - 2\sigma_b^2} \right\}, \quad \Theta^{\cos}(x, y) = \frac{1}{2} \left\{ e^{-\frac{\sigma_w^2}{2}(x - y)^2} + e^{-\frac{\sigma_w^2}{2}(x + y)^2 - 2\sigma_b^2} \right\}. \quad (\text{S25})$$

We note that the kernels (S20)(S21)(S25) are invariant under the swapping of x and y and that $-1 \leq \Theta(x, y) \leq 1$ for $\phi = \text{erf}, \sin, \cos$, since NTK is the expectation of the product of the activation functions (Eq. (S17)).

If $\sigma_b = \sigma_w = \sigma$, we obtain

$$\Theta^{\text{erf}}(x, y) = \frac{2}{\pi} \arcsin \frac{2\sigma^2(1 + xy)}{\sqrt{[1 + 2\sigma^2(1 + x^2)][1 + 2\sigma^2(1 + y^2)]}} \quad (\text{12})$$

$$\Theta^{\sin}(x, y) = \frac{1}{2} \left\{ e^{-\frac{\sigma^2}{2}(x - y)^2} - e^{-\frac{\sigma^2}{2}(x + y)^2 - 2\sigma^2} \right\} \quad (\text{13})$$

$$\Theta^{\cos}(x, y) = \frac{1}{2} \left\{ e^{-\frac{\sigma^2}{2}(x - y)^2} + e^{-\frac{\sigma^2}{2}(x + y)^2 - 2\sigma^2} \right\} \quad (\text{14})$$

$$\Theta^{\text{relu}}(x, y) = \frac{\sigma^2}{2\pi} \sqrt{(1 + x^2)(1 + y^2)} \left\{ \sqrt{1 - \frac{(1 + xy)^2}{(1 + x^2)(1 + y^2)}} + (\pi - \psi) \frac{1 + xy}{\sqrt{(1 + x^2)(1 + y^2)}} \right\} \quad (\text{15})$$

$$\text{where } \psi \equiv \arccos \frac{1 + xy}{\sqrt{(1 + x^2)(1 + y^2)}}.$$

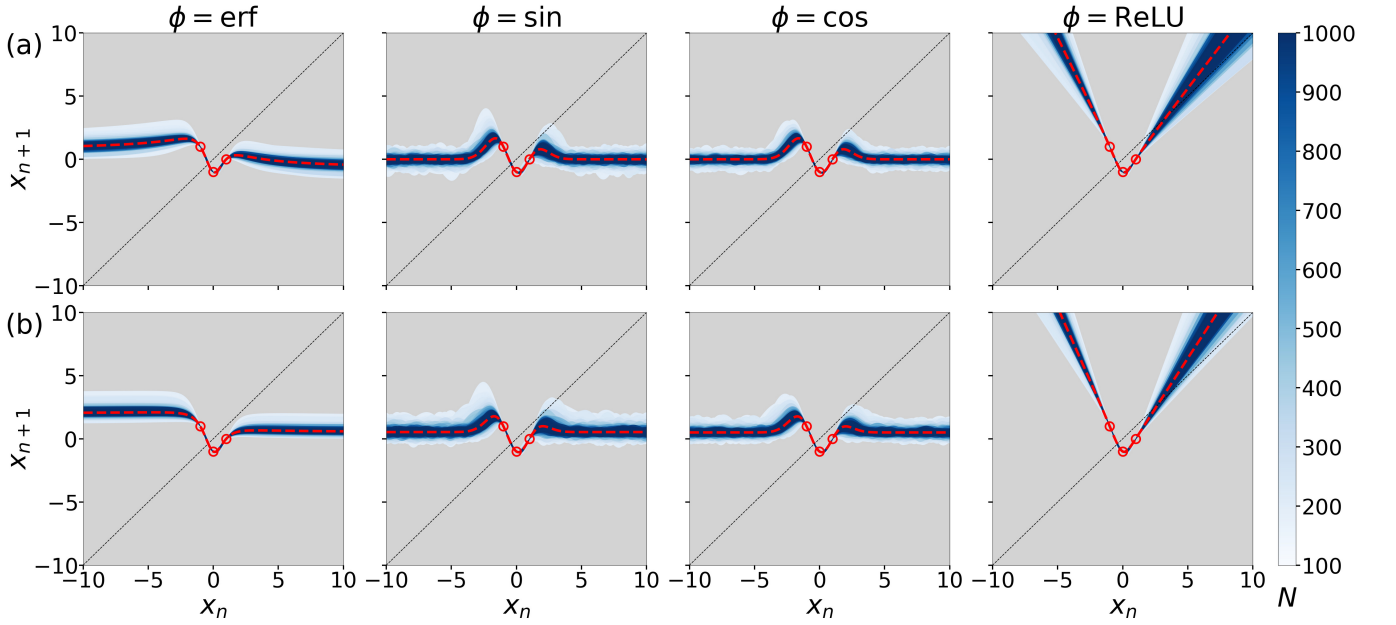


FIG. S1: Trained maps f_N^* for $\phi = \text{erf}, \sin, \cos, \text{ReLU}$ with target period three $\mathcal{D} = \{-1, 1, 0\}$ and variances of input parameters $\sigma_b^2 = \sigma_w^2 = 1.0$. The blue-colored areas indicate the maximum–minimum regions of f_N^* for 100 different realizations (a) without output bias, or (b) with output bias. The red circles and the red dotted lines show the target period three and the thermodynamic limit f_∞^* , respectively. The darkness of blue corresponds to the number of nodes N , describing that regardless of the choice of ϕ , f_N^* degenerates into f_∞^* as N increases.

The formulae of $\frac{\partial}{\partial x}\Theta(x, y)$ for $\phi = \text{erf}, \sin, \cos, \text{ReLU}$ are therefore given by

$$\frac{\partial}{\partial x}\Theta^{\text{erf}}(x, y) = \frac{4\sigma^2}{\pi [1 + 2\sigma^2(1 + x^2)]} \frac{y - 2\sigma^2(x - y)}{\sqrt{1 + 2\sigma^2(2 + x^2 + y^2) + 4\sigma^4(x - y)^2}} \quad (\text{S26})$$

$$\frac{\partial}{\partial x}\Theta^{\sin}(x, y) = -\frac{\sigma^2}{2} \left\{ (x - y)e^{-\frac{\sigma^2}{2}(x-y)^2} - (x + y)e^{-\frac{\sigma^2}{2}(x+y)^2 - 2\sigma^2} \right\} \quad (\text{S27})$$

$$\frac{\partial}{\partial x}\Theta^{\cos}(x, y) = -\frac{\sigma^2}{2} \left\{ (x - y)e^{-\frac{\sigma^2}{2}(x-y)^2} + (x + y)e^{-\frac{\sigma^2}{2}(x+y)^2 - 2\sigma^2} \right\} \quad (\text{S28})$$

$$\frac{\partial}{\partial x}\Theta^{\text{relu}}(x, y) = \frac{\sigma^2}{2\pi} \left\{ \frac{x|x - y|}{1 + x^2} + (\pi - \psi)y \right\} \quad (\text{S29})$$

where $\psi \equiv \arccos \frac{1 + xy}{\sqrt{(1 + x^2)(1 + y^2)}}$.

Eq. (15) indicates that for $\phi = \text{ReLU}$, varying σ has little effect on the trained network output (Eq. (S18)); the effect disappears in the absence of b^{out} , and increasing σ diminishes the efficacy of b^{out} in $f_\infty^{*, \text{bias}}$ ($f_\infty^{*, \text{bias}} \rightarrow f_\infty^*$). Fig. S1 shows the shape of the trained map for each activation function and how the trained network with a finite number of nodes degenerates into its unique thermodynamic limit. We observe that the choice of ϕ and the existence of b^{out} affect the shapes of the trained maps. In particular, the behavior of $f_\infty^*(x)$ for large input $|x| \gg 1$ depends strongly on the nonlinearity of the network. For $\phi = \text{erf}, \sin, \cos$, the kernels $\Theta(x, y)$, and therefore $f_\infty^*(x)$, converge to constant values as $x \rightarrow \pm\infty$:

$$\lim_{x \rightarrow \pm\infty} \Theta^{\text{erf}}(x, y) = \begin{cases} \frac{2}{\pi} \arcsin \frac{y\sqrt{2\sigma^2}}{\sqrt{1+2\sigma^2(1+y^2)}} & (x \rightarrow +\infty) \\ -\frac{2}{\pi} \arcsin \frac{y\sqrt{2\sigma^2}}{\sqrt{1+2\sigma^2(1+y^2)}} & (x \rightarrow -\infty) \end{cases} \quad (\text{S30})$$

$$\lim_{x \rightarrow \pm\infty} \Theta^{\sin}(x, y) = \lim_{x \rightarrow \pm\infty} \Theta^{\cos}(x, y) = 0. \quad (\text{S31})$$

Here, Eq. (S31) indicates that regardless of the value of σ , the trained network output $f_\infty^*(x)$ decreases to zero if x deviates largely from the target data \mathcal{D} . In contrast, $f_\infty^*(x)$ for $\phi = \text{ReLU}$ diverges as $x \rightarrow \pm\infty$.

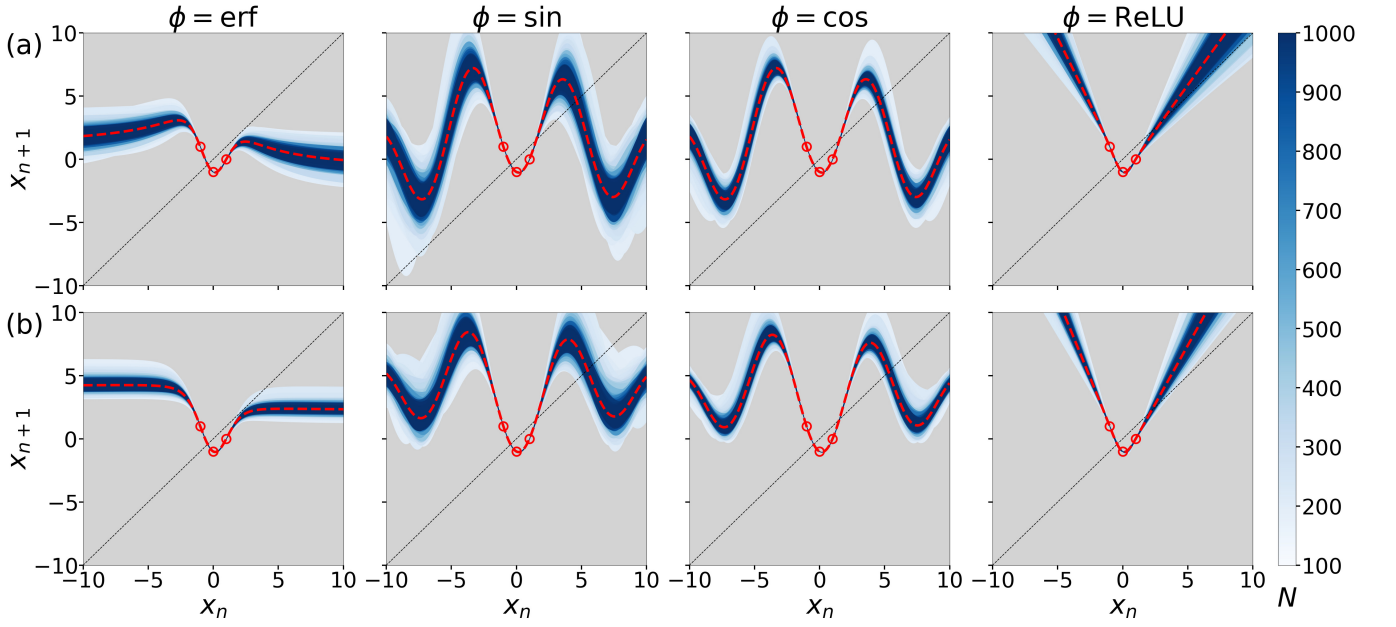


FIG. S2: Trained maps f_N^* with input parameters drawn from uniform distributions in the same setting as in Fig. S1. The choice of the probability distribution of the input layer affects the shape of the trained maps, in which we observe a significant effect for $\phi = \sin, \cos$.

C. Networks with Uniform Distributions

The kernel $\hat{\Theta}_0(x, y)$ (Eq. (S8)) with input parameters drawn from uniform distributions

$$W_i^{\text{in}} \sim \mathcal{U}(-\sigma_w, \sigma_w), \quad b_i^{\text{in}} \sim \mathcal{U}(-\sigma_b, \sigma_b) \quad (\text{S32})$$

also converges in probability to the expectation over random variables $\omega \sim \mathcal{U}(-\sigma_w, \sigma_w)$, $\beta \sim \mathcal{U}(-\sigma_b, \sigma_b)$ by the law of large numbers in the limit $N \rightarrow \infty$:

$$\begin{aligned} \hat{\Theta}_0(x, y) &\rightarrow \Theta(x, y) = \mathbb{E}[\phi(\omega x + \beta)\phi(\omega y + \beta)] = \frac{1}{4\sigma_w\sigma_b} \int_{-\sigma_b}^{\sigma_b} d\omega \int_{-\sigma_w}^{\sigma_w} d\beta \phi(\omega x + \beta)\phi(\omega y + \beta) \\ \hat{\Theta}_0^{\text{bias}}(x, y) &\rightarrow \Theta^{\text{bias}}(x, y) = \Theta(x, y) + 1. \end{aligned} \quad (\text{S33})$$

As Eq. (S33) is a definite integral, we can numerically compute NTK and, therefore, $f_\infty^*(x)$ for any input x (Fig. S2).

D. Learning with Ridge Regularization

In this subsection, we consider the continuous-time GD for the loss function with a ridge regularization term ($\lambda > 0$)

$$\mathcal{L}_{\text{ridge}} = \sum_{(x_i, y_i) \in \mathcal{D}} \frac{1}{2} \{f_t(x_i, \theta) - y_i\}^2 + \frac{\lambda}{2} \|\theta\|^2 = \frac{1}{2} \|f_t(\mathcal{X}) - \mathcal{Y}\|^2 + \frac{\lambda}{2} \|\theta\|^2 \quad (\text{S34})$$

and discuss its connection to the ridge regression in the reservoir computing (RC) scheme. Similar to IA, we obtain the following ODE of θ_t and $f_t(\mathcal{X})$ in the virtual learning dynamics:

$$\dot{\theta}_t = -\eta \nabla_{\theta} \mathcal{L}_{\text{ridge}} = -\eta [\nabla_{\theta} f_t(\mathcal{X})^{\top} \nabla_{f_t(\mathcal{X})} \mathcal{L}_{\text{ridge}} + \lambda \theta_t] = -\eta [\nabla_{\theta} f_t(\mathcal{X})^{\top} (f_t(\mathcal{X}) - \mathcal{Y}) + \lambda \theta_t] \quad (\text{S35})$$

$$\begin{aligned} \dot{f}_t(\mathcal{X}) &= \nabla_{\theta} f_t(\mathcal{X}) \dot{\theta}_t = -\eta [\nabla_{\theta} f_t(\mathcal{X}) \nabla_{f_t(\mathcal{X})} \mathcal{L}_{\text{ridge}} + \lambda \nabla_{\theta} f_t(\mathcal{X}) \theta_t] \\ &= -\eta \left[(\hat{\Theta}_0 + \lambda I) f_t(\mathcal{X}) - \hat{\Theta}_0 \mathcal{Y} \right] = -\eta \left(\hat{\Theta}_0 + \lambda I \right) \left[f_t(\mathcal{X}) - (\hat{\Theta}_0 + \lambda I)^{-1} \hat{\Theta}_0 \mathcal{Y} \right]. \end{aligned} \quad (\text{S36})$$

The solution of Eq. (S36) is given by

$$\begin{aligned} f_t(\mathcal{X}) &= e^{-\eta(\hat{\Theta}_0 + \lambda I)t} \left[f_0(\mathcal{X}) - \left(\hat{\Theta}_0 + \lambda I \right)^{-1} \hat{\Theta}_0 \mathcal{Y} \right] + \left(\hat{\Theta}_0 + \lambda I \right)^{-1} \hat{\Theta}_0 \mathcal{Y} \\ &= \left(\hat{\Theta}_0 + \lambda I \right)^{-1} \left(I - e^{-\eta(\hat{\Theta}_0 + \lambda I)t} \right) \hat{\Theta}_0 \mathcal{Y} + e^{-\eta(\hat{\Theta}_0 + \lambda I)t} f_0(\mathcal{X}). \end{aligned} \quad (\text{S37})$$

Note that the matrices $\left(\hat{\Theta}_0 + \lambda I \right)^{-1}$, $\left(I - e^{-\eta(\hat{\Theta}_0 + \lambda I)t} \right)$, and $\hat{\Theta}_0$ are simultaneously diagonalizable and commutative. Here, Eq. (S37) indicates that regardless of the initial state θ_0 and positive-definiteness of $\hat{\Theta}_0$, θ_t reaches some unique value in its learning dynamics since $e^{-\eta(\hat{\Theta}_0 + \lambda I)t} \rightarrow 0$ ($t \rightarrow \infty$):

$$f_{N,\text{ridge}}^*(\mathcal{X}) = \lim_{t \rightarrow \infty} f_t(\mathcal{X}) = \left(\hat{\Theta}_0 + \lambda I \right)^{-1} \hat{\Theta}_0 \mathcal{Y} = \hat{\Theta}_0 \left(\hat{\Theta}_0 + \lambda I \right)^{-1} \mathcal{Y}. \quad (\text{S38})$$

Moreover, we explicitly obtain the optimized parameters θ^* by taking the limit $t \rightarrow \infty$ and using $\dot{\theta}_t \rightarrow \mathbf{0}$ in Eq. (S35):

$$\begin{aligned} \mathbf{0} &= -\eta \left[\nabla_{\theta} f_0(\mathcal{X})^{\top} \left(\nabla_{\theta} f_0(\mathcal{X}) \lim_{t \rightarrow \infty} \theta_t - \mathcal{Y} \right) + \lambda \lim_{t \rightarrow \infty} \theta_t \right] \\ &= -\eta \left[\left(\nabla_{\theta} f_0(\mathcal{X})^{\top} \nabla_{\theta} f_0(\mathcal{X}) + \lambda I_{N \times N} \right) \lim_{t \rightarrow \infty} \theta_t - \nabla_{\theta} f_t(\mathcal{X})^{\top} \mathcal{Y} \right] \\ \theta_{\text{ridge}}^* &\equiv \lim_{t \rightarrow \infty} \theta_t = \left(\nabla_{\theta} f_0(\mathcal{X})^{\top} \nabla_{\theta} f_0(\mathcal{X}) + \lambda I_{N \times N} \right)^{-1} \nabla_{\theta} f_t(\mathcal{X})^{\top} \mathcal{Y}. \end{aligned} \quad (\text{S39})$$

Note that Eq. (S39) coincides with the optimized linear readout for the ridge regression in the RC scheme. Substituting Eq. (S37) into Eq. (S35), we get

$$\begin{aligned} \dot{\theta}_t &= -\eta \nabla_{\theta} f_t(\mathcal{X})^{\top} \left\{ \left(\hat{\Theta}_0 + \lambda I \right)^{-1} \left(I - e^{-\eta(\hat{\Theta}_0 + \lambda I)t} \right) \hat{\Theta}_0 \mathcal{Y} + e^{-\eta(\hat{\Theta}_0 + \lambda I)t} f_0(\mathcal{X}) - \mathcal{Y} \right\} - \eta \lambda \theta_t \\ &= -\eta \nabla_{\theta} f_t(\mathcal{X})^{\top} \left\{ \left(\hat{\Theta}_0 + \lambda I \right)^{-1} \left(\hat{\Theta}_0 + \lambda I - \lambda I - e^{-\eta(\hat{\Theta}_0 + \lambda I)t} \hat{\Theta}_0 \right) \mathcal{Y} - \mathcal{Y} + e^{-\eta(\hat{\Theta}_0 + \lambda I)t} f_0(\mathcal{X}) \right\} - \eta \lambda \theta_t \\ &= \eta \nabla_{\theta} f_t(\mathcal{X})^{\top} \left\{ \left(\hat{\Theta}_0 + \lambda I \right)^{-1} \left(\lambda I + e^{-\eta(\hat{\Theta}_0 + \lambda I)t} \hat{\Theta}_0 \right) \mathcal{Y} - e^{-\eta(\hat{\Theta}_0 + \lambda I)t} f_0(\mathcal{X}) \right\} - \eta \lambda \theta_t. \end{aligned} \quad (\text{S40})$$

Combining Eq. (S40) with $\dot{f}_t(x, \theta) = \nabla_{\theta} f_t(x, \theta) \dot{\theta}_t$, and $f_t(x, \theta) = \nabla_{\theta} f_t(x, \theta) \theta_t = \nabla_{\theta} f_0(x, \theta) \theta_t$, we get

$$\dot{f}_t(x, \theta) = \nabla_{\theta} f_t(x, \theta) \dot{\theta}_t = \eta \hat{\Theta}_0(x, \mathcal{X}) \left\{ \left(\hat{\Theta}_0 + \lambda I \right)^{-1} \left(\lambda I + e^{-\eta(\hat{\Theta}_0 + \lambda I)t} \hat{\Theta}_0 \right) \mathcal{Y} - e^{-\eta(\hat{\Theta}_0 + \lambda I)t} f_0(\mathcal{X}) \right\} - \eta \lambda f_t(x, \theta). \quad (\text{S41})$$

Similarly, we can obtain the trained network output in ridge regression $f_N^*(x)$ by taking the limit $t \rightarrow \infty$ in Eq. (S41):

$$\begin{aligned} 0 &= \eta \lambda \hat{\Theta}_0(x, \mathcal{X}) \left(\hat{\Theta}_0 + \lambda I \right)^{-1} \mathcal{Y} - \eta \lambda \lim_{t \rightarrow \infty} f_t(x, \theta) \\ f_{N,\text{ridge}}^*(x) &\equiv \lim_{t \rightarrow \infty} f_t(x, \theta) = \hat{\Theta}_0(x, \mathcal{X}) \left(\hat{\Theta}_0 + \lambda I \right)^{-1} \mathcal{Y}. \end{aligned} \quad (\text{S42})$$

Assuming that $\theta_0 = \mathbf{0}$ allows us to obtain the explicit formulae of the learning dynamics of θ_t and $f_t(x, \theta)$:

$$\theta_t|_{\theta_0=\mathbf{0}} = \nabla_{\theta} f_t(\mathcal{X})^{\top} \left(\hat{\Theta}_0 + \lambda I \right)^{-1} \left(I - e^{-\eta(\hat{\Theta}_0 + \lambda I)t} \right) \mathcal{Y} \quad (\text{S43})$$

$$f_t(x, \theta)|_{\theta_0=\mathbf{0}} = \hat{\Theta}_0(x, \mathcal{X}) \left(\hat{\Theta}_0 + \lambda I \right)^{-1} \left(I - e^{-\eta(\hat{\Theta}_0 + \lambda I)t} \right) \mathcal{Y}. \quad (\text{S44})$$

We note that a similar formula of $f_t(x, \theta)$ has appeared in Sec. 5.3 in Ref. [9] via discrete-time GD with $\theta_0 = \mathbf{0}$. We acquire the thermodynamic limit of the trained network output by again using NTK, since $f_N^*(x)$ (Eq. (S42)) is calculated from only the values of the kernel $\hat{\Theta}_0(x, y)$:

$$f_{\infty,\text{ridge}}^*(x) = \Theta(x, \mathcal{X}) (\Theta + \lambda I)^{-1} \mathcal{Y}. \quad (\text{S45})$$

Here, Eq. (S45) coincides with the network output in kernel ridge regression [10–12] and Eq. (7) in the limit $\lambda \rightarrow 0^+$. Most notably, Eq. (S45) indicates that λ acts as the bifurcation parameter of the embeddable attractors; the change in the learning machine dynamics with respect to λ is also described by the bifurcation of the characteristic attractors.

II. FINITENESS OF THE ATTRACTORS OF THE TRAINED MAP WITH THE BOUNDED ANALYTIC NTK

Regarding a smooth map from a finite interval I to itself, there is a significant theorem on the number of its attractors [13]:

Theorem S1. (Melo–Strien) *If $f : I \rightarrow I$ is a C^2 map with non-flat critical points, then there exist $\lambda > 1$ and $n_0 \in \mathbb{N}$ such that*

$$\left| \frac{d}{dx} f^n(p) \right| > \lambda \quad (\text{S46})$$

for every periodic point p of f of period $n \geq n_0$.

Here, we say that $c \in I$ is a critical point if it satisfies $\frac{d}{dx} f(c) = 0$, and that a critical point c for a smooth map is non-flat if there exists $k \geq 2$ such that $\frac{d^k}{dx^k} f(c) \neq 0$ [13, 14]. Note that if f is a non-constant analytic map with critical points, then all critical points are non-flat since $f(x)$ has the Taylor expansion for every $x_0 \in I$, and its coefficients for some $k \geq 2$ degrees are non-zero [14]. Hence, we obtain the following corollary of Theorem S1:

Corollary S2. *If $f : I \rightarrow I$ is a non-constant analytic map with critical points, then there exist $\lambda > 1$ and $n_0 \in \mathbb{N}$ such that*

$$\left| \frac{d}{dx} f^n(p) \right| > \lambda \quad (\text{S47})$$

for every periodic point p of f of period $n \geq n_0$.

For our neural network model, if the kernels $\hat{\Theta}_0(x, y)$ and $\Theta(x, y)$ are bounded and analytic (e.g., $\phi = \text{erf}, \sin, \cos$), then the network outputs are also bounded and analytic since $f_N^*(x)$ (Eq. (S16)) and $f_\infty^*(x)$ (Eq. (S18)) are described by the weighted sum of the kernels. Further, in learning period $n \geq 2$, $f_N^*(x)$ and $f_\infty^*(x)$ with positive definite matrices $\hat{\Theta}_0$ and Θ , respectively, cannot be constant functions because, otherwise, they will not be able to replicate the target input–output pairs \mathcal{D} . In addition, in learning period three, f_N^* and f_∞^* have at least one critical point by their folding around \mathcal{D} and Rolle’s theorem; we can restrict the bounded f_N^* and f_∞^* to some finite interval that contains all the periods and critical points. Therefore, if $\hat{\Theta}_0(x, y)$ and $\Theta(x, y)$ are bounded and analytic, then f_N^* and f_∞^* in learning period three has at most finitely many stable periods (attractors) by Corollary S2.

III. SYMMETRIES IN LEARNING PERIOD THREE

In this section, we describe that the characteristic bifurcation structure in learning period three ($\mathcal{D} = \{a, b, c\}$) has two types of universal symmetry properties derived from the symmetry of $\{a, b, c\}$ under the swapping of a and b (Fig. S3). For the sake of simplicity, we assume $a < b$ with a and b fixed. One symmetry is the inverted structure near the singular points $c = a$ and $c = b$:

$$\begin{aligned} \lim_{c \nearrow a} f_\infty^*(x)|_{\mathcal{D}=\{a,b,c\}} &= \lim_{c \searrow a} f_\infty^*(x)|_{\mathcal{D}=\{b,a,c\}} \\ \lim_{c \searrow b} f_\infty^*(x)|_{\mathcal{D}=\{a,b,c\}} &= \lim_{c \nearrow b} f_\infty^*(x)|_{\mathcal{D}=\{b,a,c\}}. \end{aligned} \quad (\text{S48})$$

The left-hand side of Eq. (S48) corresponds to the outside structure ($c < a, b < c$), and the right-hand side of Eq. (S48) corresponds to the inside structure ($a < c < b$) with the other type of target period three (Fig. S4). The other symmetry is, for the specific case of $b \approx -a$ and $\Theta(x, y) = \Theta(-x, -y)$, the inversion of the whole bifurcation structure under the swapping of a and b :

$$f_\infty^*(x)|_{\mathcal{D}=\{a,b,c\}} \simeq -f_\infty^*(-x + a + b)|_{\mathcal{D}=\{b,a,-c+a+b\}} + a + b, \quad (\text{S49})$$

where the symbol \simeq in Eq. (S49) means that the shapes of two maps are similar when $b \approx -a$ (Fig. S5). Note that the following equation always holds on target period three even if $\Theta(x, y) \neq \Theta(-x, -y)$:

$$f_\infty^*(p)|_{\mathcal{D}=\{a,b,c\}} = -f_\infty^*(-p + a + b)|_{\mathcal{D}=\{b,a,-c+a+b\}} + a + b \quad (p = a, b, c). \quad (\text{S50})$$

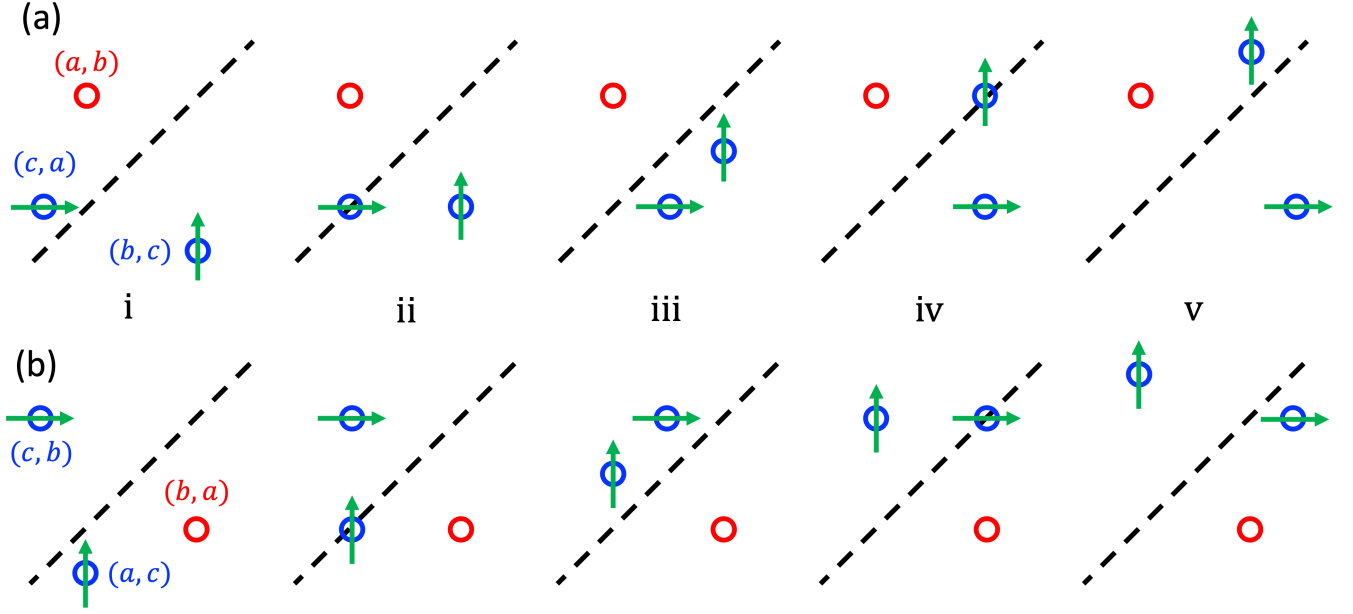


FIG. S3: Symmetry of target period three. (a) $\mathcal{D} = \{a, b, c\}$. (b) $\mathcal{D} = \{b, a, c\}$. The five regions (i)–(v) show the Poincaré plots in (i) $c < a$, (ii) $c = a$, (iii) $a < c < b$, (iv) $c = b$, and (v) $b < c$, respectively. The dotted lines correspond to $x_{n+1} = x_n$. The circles indicate target period three, and the red circles indicate a c -independent point (a, b) or (b, a) . The green arrows represent the moving direction of \mathcal{D} as c increases. The one-to-one correspondences (a)(ii)–(b)(ii) and (a)(iv)–(b)(iv) create the symmetry of Eq. (S48). Rotating the plots in (b) 180 degrees about $(\frac{a+b}{2}, \frac{a+b}{2})$ and transforming c to $-c + a + b$ makes the same plots as in (a) (Eq. (S50)).

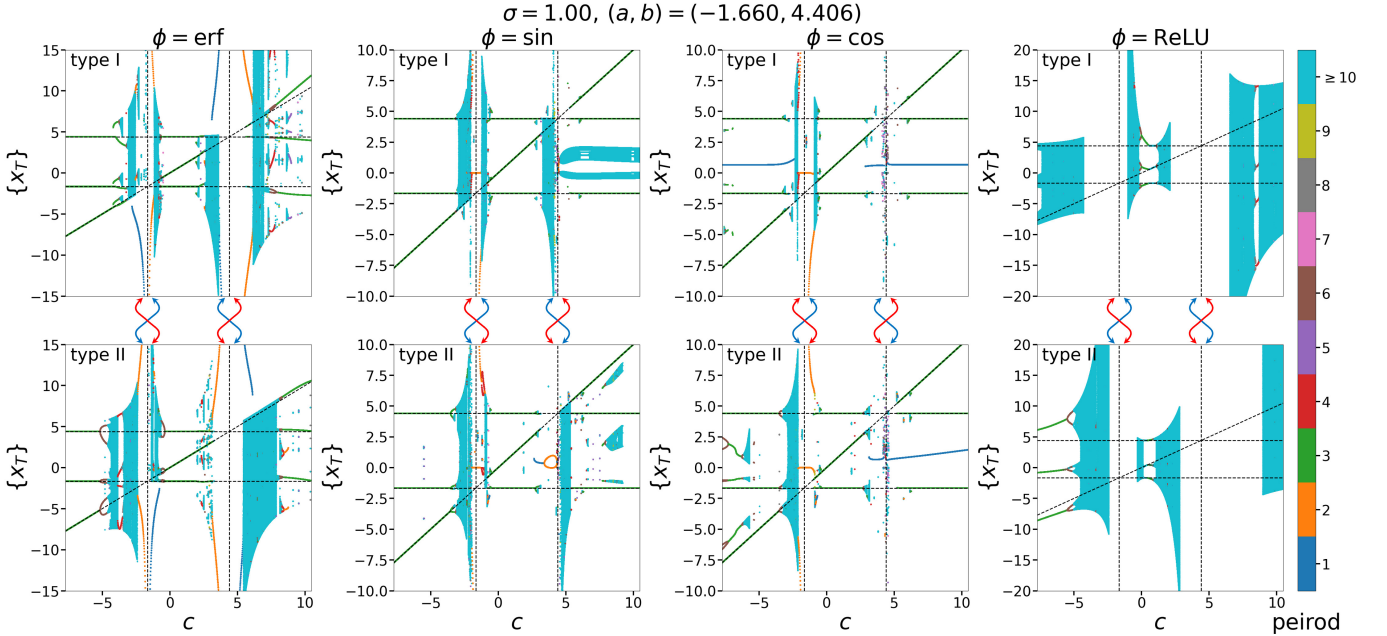


FIG. S4: Symmetry of Eq. (S48). Characteristic bifurcation structures of the dynamical systems $f_{\infty}^*|_{\mathcal{D}=\{a,b,c\}}$ (type I) and $f_{\infty}^*|_{\mathcal{D}=\{b,a,c\}}$ (type II) with respect to c . The dotted lines indicate target period three; the diagonal lines correspond to a varying c . The red arrows (or the blue arrows) indicate the qualitative correspondence between the outside structure ($c < a, b < c$) of type I (or type II) and the inside structure ($a < c < b$) of type II (or type I).

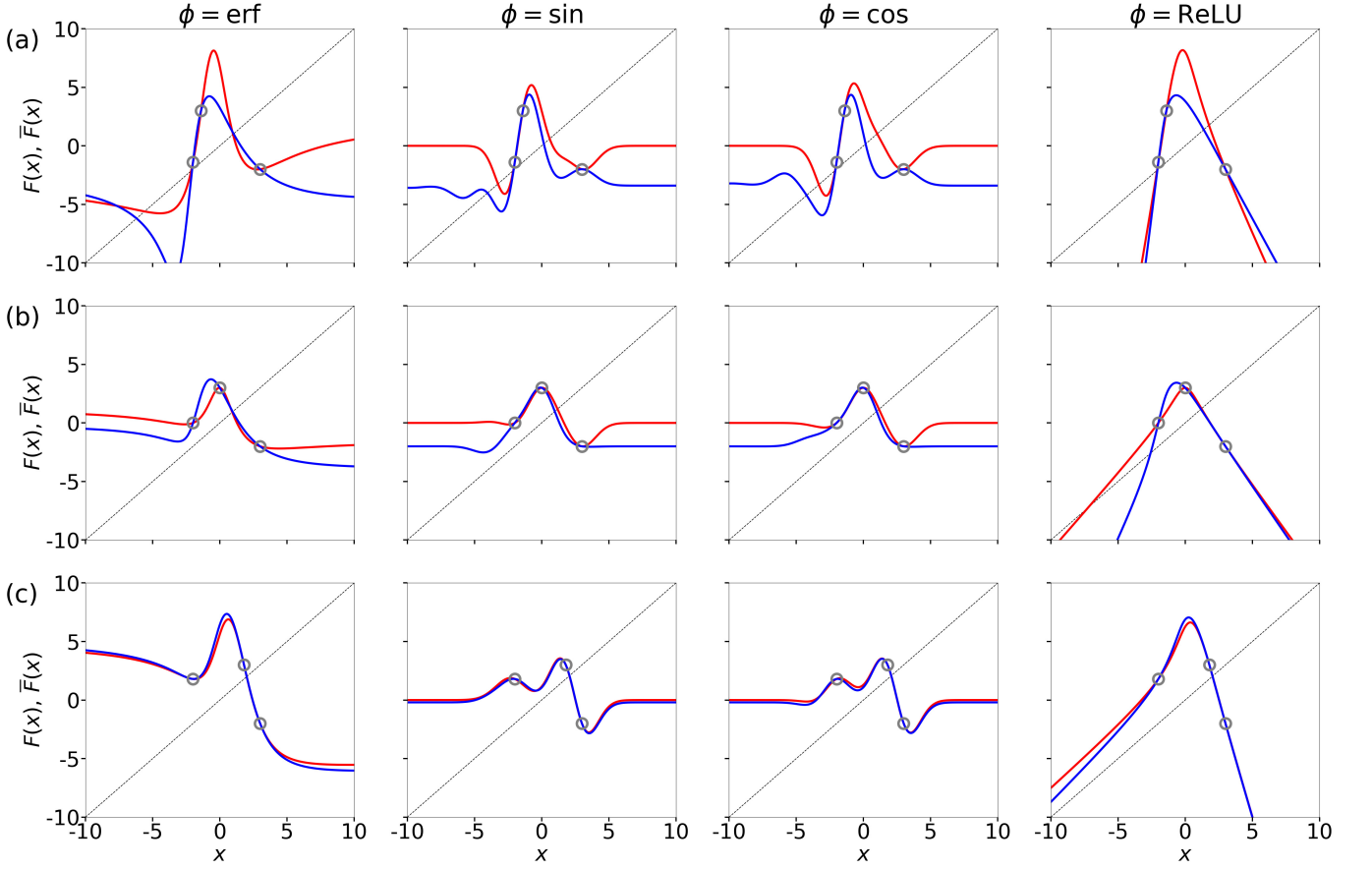


FIG. S5: Symmetry of Eq. (S49). $\{a, b, c\} =$ (a) $\{-2.0, -1.2, 3.0\}$, (b) $\{-2.0, 0.0, 3.0\}$, (c) $\{-2.0, 1.8, 3.0\}$, with fixed input intensity $\sigma = 1.0$. The circles indicate target period three. The red and blue lines indicate $g(x) \equiv f_{\infty}^*|_{\mathcal{D}=\{a,b,c\}}$ and $\bar{g}(x) \equiv -f_{\infty}^*(-x+a+b)|_{\mathcal{D}=\{b,a,-c+a+b\}} + a+b$, respectively. As b approaches $-a$, the symmetry around $x = a, b, c$ (Eq. (S50)) spreads throughout $x \in \mathbb{R}$ (Eq. (S57)) if $\Theta(x, y) = \Theta(-x, -y)$.

By combining these two symmetries (Eqs. (S48) and (S49)), we can qualitatively infer the outside structure only from the bifurcation diagram in the inside region if $b \approx -a$ (Fig. 2(a),(b)).

In the following we show the proof of Eq. (S49), restricting to the case of $b = -a$. Combining Eq. (S18) with $\Theta(x, y) = \Theta(y, x)$, $f_{\infty}^*(x)|_{\mathcal{D}=\{a,b,c\}}$ is given by

$$\begin{aligned}
 f_{\infty}^*(x)|_{\mathcal{D}=\{a,b,c\}} &= \frac{b}{|\Theta|} [\Theta(x, a) \{ \Theta(b, b)\Theta(c, c) - \Theta(b, c)^2 \} \\
 &\quad + \Theta(x, b) \{ \Theta(b, c)\Theta(c, a) - \Theta(a, b)\Theta(c, c) \} \\
 &\quad + \Theta(x, c) \{ \Theta(a, b)\Theta(b, c) - \Theta(b, b)\Theta(c, a) \}] \\
 &\quad + \frac{c}{|\Theta|} [\Theta(x, a) \{ \Theta(b, c)\Theta(c, a) - \Theta(a, b)\Theta(c, c) \} \\
 &\quad + \Theta(x, b) \{ \Theta(c, c)\Theta(a, a) - \Theta(c, a)^2 \} \\
 &\quad + \Theta(x, c) \{ \Theta(a, b)\Theta(c, a) - \Theta(a, a)\Theta(b, c) \}] \\
 &\quad + \frac{a}{|\Theta|} [\Theta(x, a) \{ \Theta(a, b)\Theta(b, c) - \Theta(b, b)\Theta(c, a) \} \\
 &\quad + \Theta(x, b) \{ \Theta(a, b)\Theta(c, a) - \Theta(a, a)\Theta(b, c) \} \\
 &\quad + \Theta(x, c) \{ \Theta(a, a)\Theta(b, b) - \Theta(a, b)^2 \}]
 \end{aligned} \tag{S51}$$

$$|\Theta| = \Theta(a, a)\Theta(b, b)\Theta(c, c) + 2\Theta(a, b)\Theta(b, c)\Theta(c, a) - \Theta(a, a)\Theta(b, c)^2 - \Theta(b, b)\Theta(c, a)^2 - \Theta(c, c)\Theta(a, b)^2. \tag{S52}$$

Applying $b = -a$ and $\Theta(x, y) = \Theta(-x, -y)$ to Eqs. (S51) and (S52), we get

$$\begin{aligned}
f_{\infty}^*(x)|_{\mathcal{D}=\{a,-a,c\}} &= -\frac{a}{|\Theta|} [\Theta(x, a) \{ \Theta(a, a)\Theta(c, c) - \Theta(c, -a)^2 \} \\
&\quad + \Theta(x, -a) \{ \Theta(c, -a)\Theta(c, a) - \Theta(a, -a)\Theta(c, c) \} \\
&\quad + \Theta(x, c) \{ \Theta(a, -a)\Theta(c, -a) - \Theta(a, a)\Theta(c, a) \}] \\
&\quad + \frac{c}{|\Theta|} [\Theta(x, a) \{ \Theta(c, -a)\Theta(c, a) - \Theta(a, -a)\Theta(c, c) \} \\
&\quad + \Theta(x, -a) \{ \Theta(c, c)\Theta(a, a) - \Theta(c, a)^2 \} \\
&\quad + \Theta(x, c) \{ \Theta(a, -a)\Theta(c, a) - \Theta(a, a)\Theta(c, -a) \}] \\
&\quad + \frac{a}{|\Theta|} [\Theta(x, a) \{ \Theta(a, -a)\Theta(c, -a) - \Theta(a, a)\Theta(c, a) \} \\
&\quad + \Theta(x, -a) \{ \Theta(a, -a)\Theta(c, a) - \Theta(a, a)\Theta(c, -a) \} \\
&\quad + \Theta(x, c) \{ \Theta(a, a)^2 - \Theta(a, -a)^2 \}]
\end{aligned} \tag{S53}$$

$$|\Theta| = \Theta(a, a)^2\Theta(c, c) + 2\Theta(a, -a)\Theta(c, a)\Theta(c, -a) - \Theta(a, a) \{ \Theta(c, a)^2 + \Theta(c, -a)^2 \} - \Theta(c, c)\Theta(a, -a)^2. \tag{S54}$$

We note that $|\Theta|$ (Eq. (S54)) is invariant under the sign change of a or c ($a \rightarrow -a, c \rightarrow -c$). Now, let us consider the other type of learning period three ($\mathcal{D} = \{-a, a, c\}$), i.e., the sign change of a :

$$\begin{aligned}
f_{\infty}^*(x)|_{\mathcal{D}=\{-a,a,c\}} &= \frac{a}{|\Theta|} [\Theta(x, -a) \{ \Theta(a, a)\Theta(c, c) - \Theta(c, a)^2 \} \\
&\quad + \Theta(x, a) \{ \Theta(c, a)\Theta(c, -a) - \Theta(a, -a)\Theta(c, c) \} \\
&\quad + \Theta(x, c) \{ \Theta(a, -a)\Theta(c, a) - \Theta(a, a)\Theta(c, -a) \}] \\
&\quad + \frac{c}{|\Theta|} [\Theta(x, -a) \{ \Theta(c, a)\Theta(c, -a) - \Theta(a, -a)\Theta(c, c) \} \\
&\quad + \Theta(x, a) \{ \Theta(c, c)\Theta(a, a) - \Theta(c, -a)^2 \} \\
&\quad + \Theta(x, c) \{ \Theta(a, -a)\Theta(c, -a) - \Theta(a, a)\Theta(c, a) \}] \\
&\quad - \frac{a}{|\Theta|} [\Theta(x, -a) \{ \Theta(a, -a)\Theta(c, a) - \Theta(a, a)\Theta(c, -a) \} \\
&\quad + \Theta(x, a) \{ \Theta(a, -a)\Theta(c, -a) - \Theta(a, a)\Theta(c, a) \} \\
&\quad + \Theta(x, c) \{ \Theta(a, a)^2 - \Theta(a, -a)^2 \}].
\end{aligned} \tag{S55}$$

Applying the transformation $x \rightarrow -x$ and $c \rightarrow -c$ to Eq. (S55), we obtain

$$\begin{aligned}
f_{\infty}^*(-x)|_{\mathcal{D}=\{-a,a,-c\}} &= \frac{a}{|\Theta|} [\Theta(x, a) \{ \Theta(a, a)\Theta(c, c) - \Theta(c, -a)^2 \} \\
&\quad + \Theta(x, -a) \{ \Theta(c, -a)\Theta(c, a) - \Theta(a, -a)\Theta(c, c) \} \\
&\quad + \Theta(x, c) \{ \Theta(a, -a)\Theta(c, -a) - \Theta(a, a)\Theta(c, a) \}] \\
&\quad - \frac{c}{|\Theta|} [\Theta(x, a) \{ \Theta(c, -a)\Theta(c, a) - \Theta(a, -a)\Theta(c, c) \} \\
&\quad + \Theta(x, -a) \{ \Theta(c, c)\Theta(a, a) - \Theta(c, a)^2 \} \\
&\quad + \Theta(x, c) \{ \Theta(a, -a)\Theta(c, a) - \Theta(a, a)\Theta(c, -a) \}] \\
&\quad - \frac{a}{|\Theta|} [\Theta(x, a) \{ \Theta(a, -a)\Theta(c, -a) - \Theta(a, a)\Theta(c, a) \} \\
&\quad + \Theta(x, -a) \{ \Theta(a, -a)\Theta(c, a) - \Theta(a, a)\Theta(c, -a) \} \\
&\quad + \Theta(x, c) \{ \Theta(a, a)^2 - \Theta(a, -a)^2 \}].
\end{aligned} \tag{S56}$$

Eqs. (S53) and (S56) yield

$$f_{\infty}^*(x)|_{\mathcal{D}=\{a,-a,c\}} = -f_{\infty}^*(-x)|_{\mathcal{D}=\{-a,a,-c\}}, \tag{S57}$$

which is what we wanted to prove. Note that the attractors of the dynamical system f_{∞}^* also have the symmetry (S57) as

$$F^n(x) = F^{n-1} \circ -\overline{F}(-x) = \dots = -\overline{F}^n(-x), \quad \text{where } F(x) \equiv f_{\infty}^*(x)|_{\mathcal{D}=\{a,-a,c\}} \quad \text{and} \quad \overline{F}(x) \equiv f_{\infty}^*(x)|_{\mathcal{D}=\{-a,a,-c\}}.$$

IV. LEARNING MACHINE DYNAMICS FOR $\phi = \text{erf}, \text{sin}, \text{cos}, \text{ReLU}$

In this section, we show the characteristic bifurcation structures in learning period three for $\phi = \text{erf}, \text{sin}, \text{cos}, \text{ReLU}$ and discuss how the choice of \mathcal{D} , ϕ , and σ affects the characteristic attractors. Hereafter, we restrict ourselves to the analysis of the bifurcation in $a < c < -a$ with $\mathcal{D} = \{a, -a, c\}$, considering the symmetry properties of Eqs. (S48) and (S49).

Figures S6 and S7 show the one-dimensional bifurcation diagrams with respect to c , and Figs. S8 and S9 show the two-dimensional bifurcation diagrams with respect to c and σ . The nonlinearity ϕ changes the dependence of f_∞^* (or $f_\infty^{*,\text{bias}}$) on \mathcal{D} and σ , resulting in the broad diversity of the characteristic bifurcation structure. We note that the wavy deviations of f_N^* from f_∞^* cause the finite-size effects, in which we observe the attractors not appearing in the characteristic bifurcation structure (Fig. S10).

The explicit formula of NTK (e.g., Eqs. (12)–(15)) allows us to obtain the infinite input-intensity limit of learning machines. Although the limit $\sigma \rightarrow \infty$ has no significant effect for $\phi = \text{ReLU}$ as the corresponding kernel is (almost) σ -independent, the trained maps for $\phi = \text{erf}, \text{sin}, \text{cos}$ qualitatively change in this limit (Fig. S11). For $\phi = \text{erf}$, f_∞^* becomes piecewise-monotonic and piecewise-smooth:

$$\lim_{\sigma \rightarrow \infty} \Theta^{\text{erf}}(x, y) = \frac{2}{\pi} \arcsin \frac{1 + xy}{\sqrt{(1 + x^2)(1 + y^2)}} \quad (\text{S17})$$

$$\frac{\partial}{\partial x} \lim_{\sigma \rightarrow \infty} \Theta^{\text{erf}}(x, y) = \frac{-2}{\pi(1 + x^2)} \cdot \frac{x - y}{|x - y|} = \begin{cases} \frac{2}{\pi} \cdot \frac{1}{1 + x^2} & (x < y) \\ -\frac{2}{\pi} \cdot \frac{1}{1 + x^2} & (x > y) \end{cases}, \quad (\text{S58})$$

since the sign of the derivative $\frac{d}{dx} \lim_{\sigma \rightarrow \infty} f_\infty^*(x)$ depends only on the magnitude relation between the input x and data point y . For $\phi = \text{sin}, \text{cos}$, the trained maps become the discontinuous functions that behave as constant functions except at \mathcal{D} :

$$\lim_{\sigma \rightarrow \infty} \Theta^{\text{sin}}(x, y) = \lim_{\sigma \rightarrow \infty} \Theta^{\text{cos}}(x, y) = \frac{1}{2} \mathbf{1}_y(x) \quad \text{where} \quad \mathbf{1}_y(x) \equiv \begin{cases} 1 & (x = y) \\ 0 & (\text{otherwise}) \end{cases} \quad (\text{S59})$$

$$\lim_{\sigma \rightarrow \infty} f_\infty^{*,\text{sin}}(x) = \lim_{\sigma \rightarrow \infty} f_\infty^{*,\text{cos}}(x) = \frac{1}{2} [\mathbf{1}_a(x) \quad \mathbf{1}_b(x) \quad \mathbf{1}_c(x)] (2I) \begin{bmatrix} b \\ c \\ a \end{bmatrix} = b\mathbf{1}_a(x) + c\mathbf{1}_b(x) + a\mathbf{1}_c(x) \quad (\text{S60})$$

$$\lim_{\sigma \rightarrow \infty} f_\infty^{*,\text{sin}}(\mathcal{X}) = \lim_{\sigma \rightarrow \infty} f_\infty^{*,\text{cos}}(\mathcal{X}) = \mathcal{Y}, \quad \lim_{\sigma \rightarrow \infty} f_\infty^{*,\text{sin}}(x) = \lim_{\sigma \rightarrow \infty} f_\infty^{*,\text{cos}}(x) = 0 \quad (x \notin \{a, b, c\}). \quad (\text{S61})$$

In particular for $\phi = \text{erf}$, we can restrict the trained map to the interval $I = [\min\{a, b, c\}, \max\{a, b, c\}]$; therefore, $\lim_{\sigma \rightarrow \infty} f_\infty^*(x)$ has all the periods in I by Sharkovsky's and Li–Yorke's theorems. Interestingly, the candidate of robust chaos [15, 16] appears for some choices of \mathcal{D} (Fig. S11 (b)). This remarkable phenomenon is caused by the step-function-like behavior of $\text{erf}(\sigma x)$ for large σ . Actually, in the limit $N \rightarrow \infty, \sigma \rightarrow \infty$, NTK for sigmoidal activation is equivalent to that for binary activation ($\phi = \text{sgn}$) [17]:

$$\Theta^{\text{sgn}}(x, y) = \frac{2}{\pi} \arcsin \frac{1 + xy}{\sqrt{(1 + x^2)(1 + y^2)}} = \lim_{\sigma \rightarrow \infty} \Theta^{\text{erf}}(x, y). \quad (\text{S62})$$

More importantly, despite the discontinuity of $\phi = \text{sgn}$, the trained network output $f_\infty^*(x)$ becomes continuous in the thermodynamic limit. Namely, f_N^* for $\phi = \text{sgn}$ is in the range of Sharkovsky's and Li–Yorke's theorems only when $N \rightarrow \infty$, resulting in the finite-size effects of the learning machine (Fig. S12).

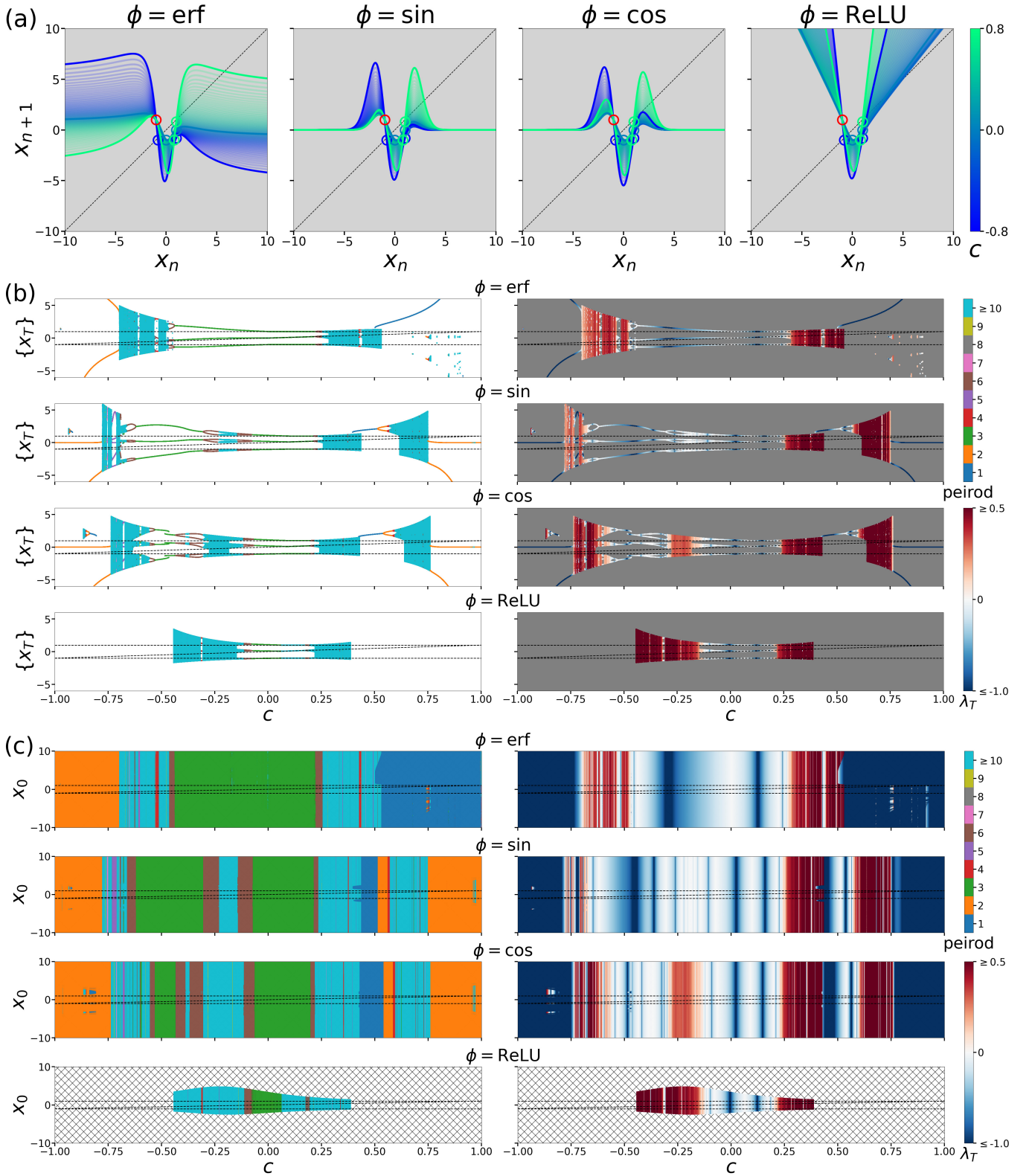


FIG. S6: One-dimensional bifurcation diagrams of the characteristic attractors of the dynamical system f_∞^* with respect to c , with $a = -1$, $b = 1$, $\sigma = 1.0$, and $T = 10^5$. (a) Change in the map f_∞^* in $-0.8 \leq c \leq 0.8$. (b) Change in the characteristic attractors calculated with $-10 \leq x_0 \leq 10$. (c) Change in the basin of attraction. The black-hatched area indicates the region (c, x_0) , where the trajectory heads toward infinity.

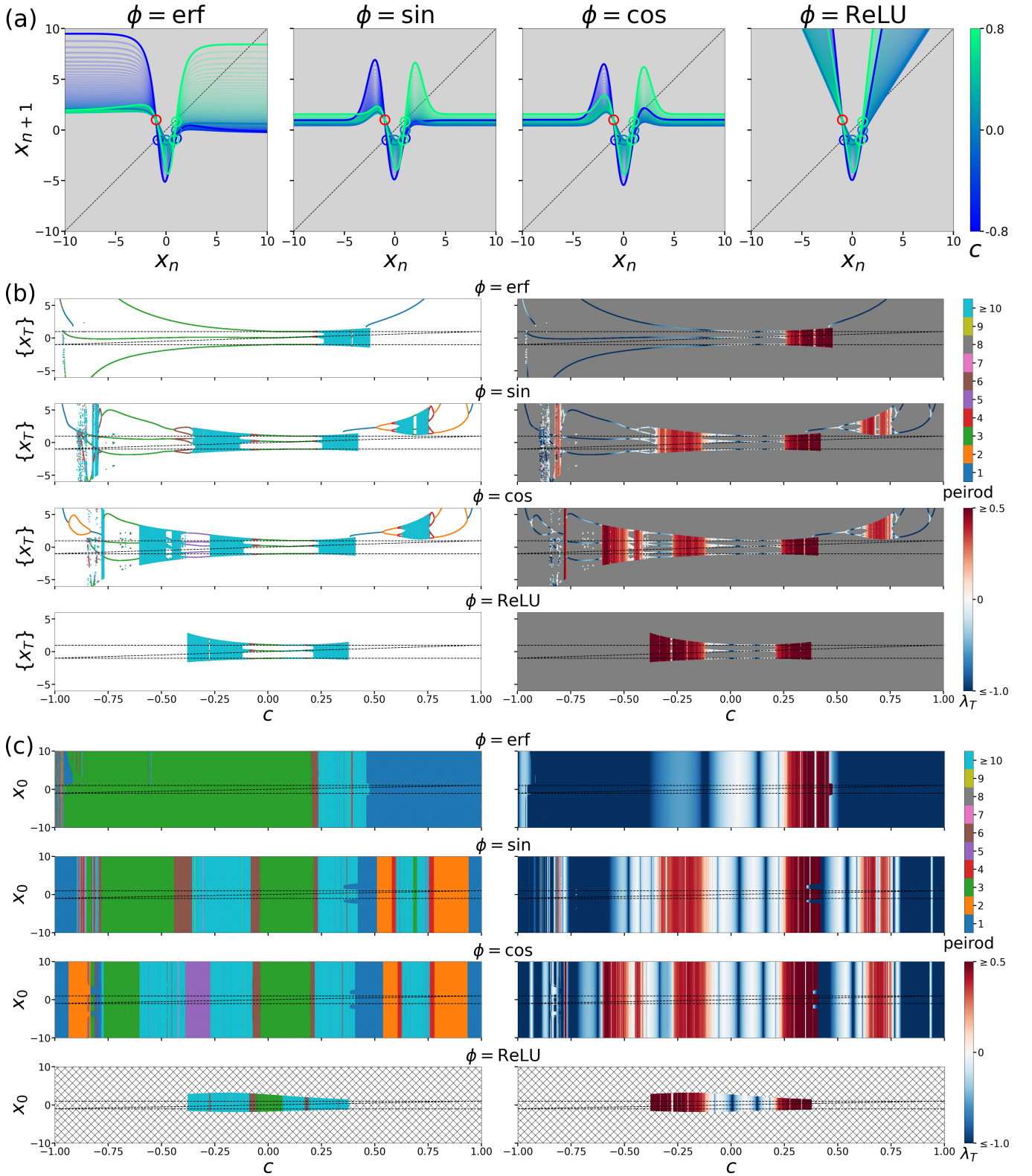


FIG. S7: One-dimensional bifurcation diagrams of the characteristic attractors of the dynamical system $f_\infty^{*,\text{bias}}$ with respect to c , with $a = -1$, $b = 1$, $\sigma = 1.0$, and $T = 10^5$. (a) Change in the map $f_\infty^{*,\text{bias}}$ in $-0.8 \leq c \leq 0.8$. (b) Change in the characteristic attractors calculated with $-10 \leq x_0 \leq 10$. (c) Change in the basin of attraction. The black-hatched area indicates the region (c, x_0) , where the trajectory heads toward infinity.

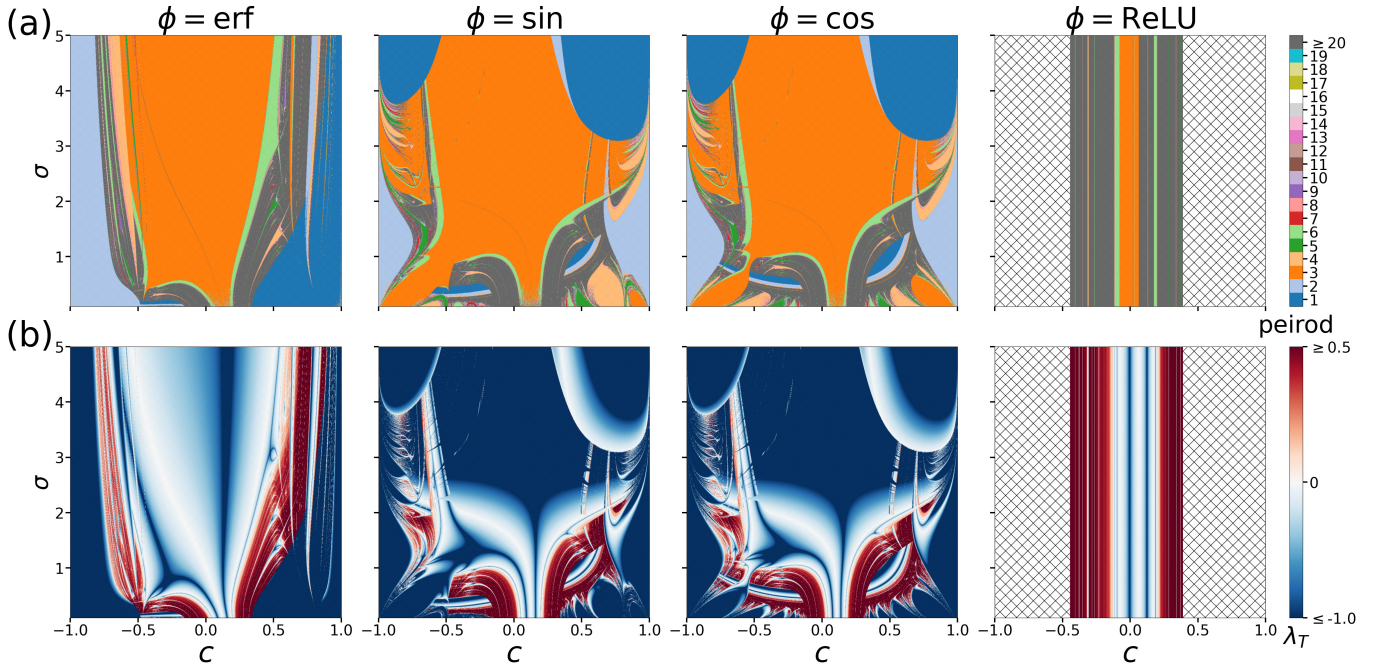


FIG. S8: Two-dimensional slices of the characteristic bifurcation structure of the dynamical system f_∞^* with respect to c and σ , with $a = -1$, $b = 1$, $x_0 = 0$, and $T = 10^4$. (a) Period of attractors. (b) Lyapunov exponents. The black-hatched area indicates the region (c, σ) , where the trajectory starting from $x_0 = 0$ heads toward infinity.

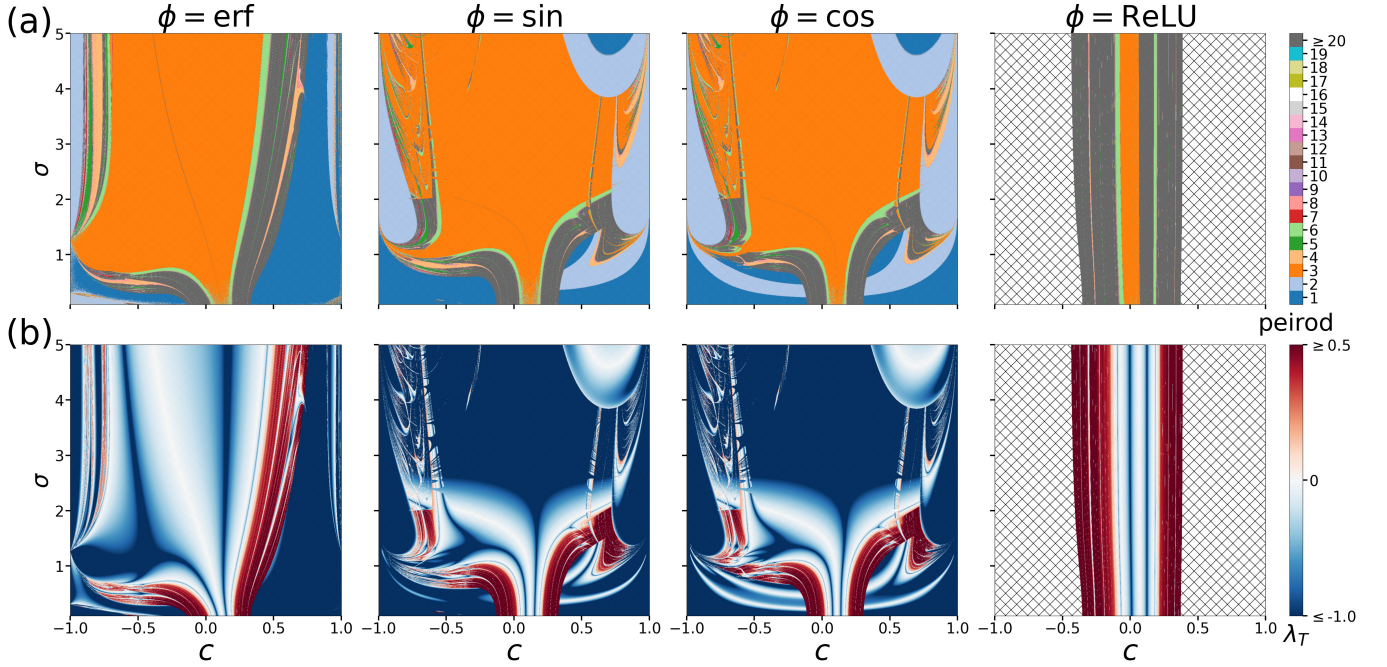


FIG. S9: Two-dimensional slices of the characteristic bifurcation structure of the dynamical system $f_\infty^{*,\text{bias}}$ with respect to c and σ , with $a = -1$, $b = 1$, $x_0 = 0$, and $T = 10^4$. (a) Period of attractors. (b) Lyapunov exponents. The black-hatched area indicates the region (c, σ) , where the trajectory starting from $x_0 = 0$ heads toward infinity.

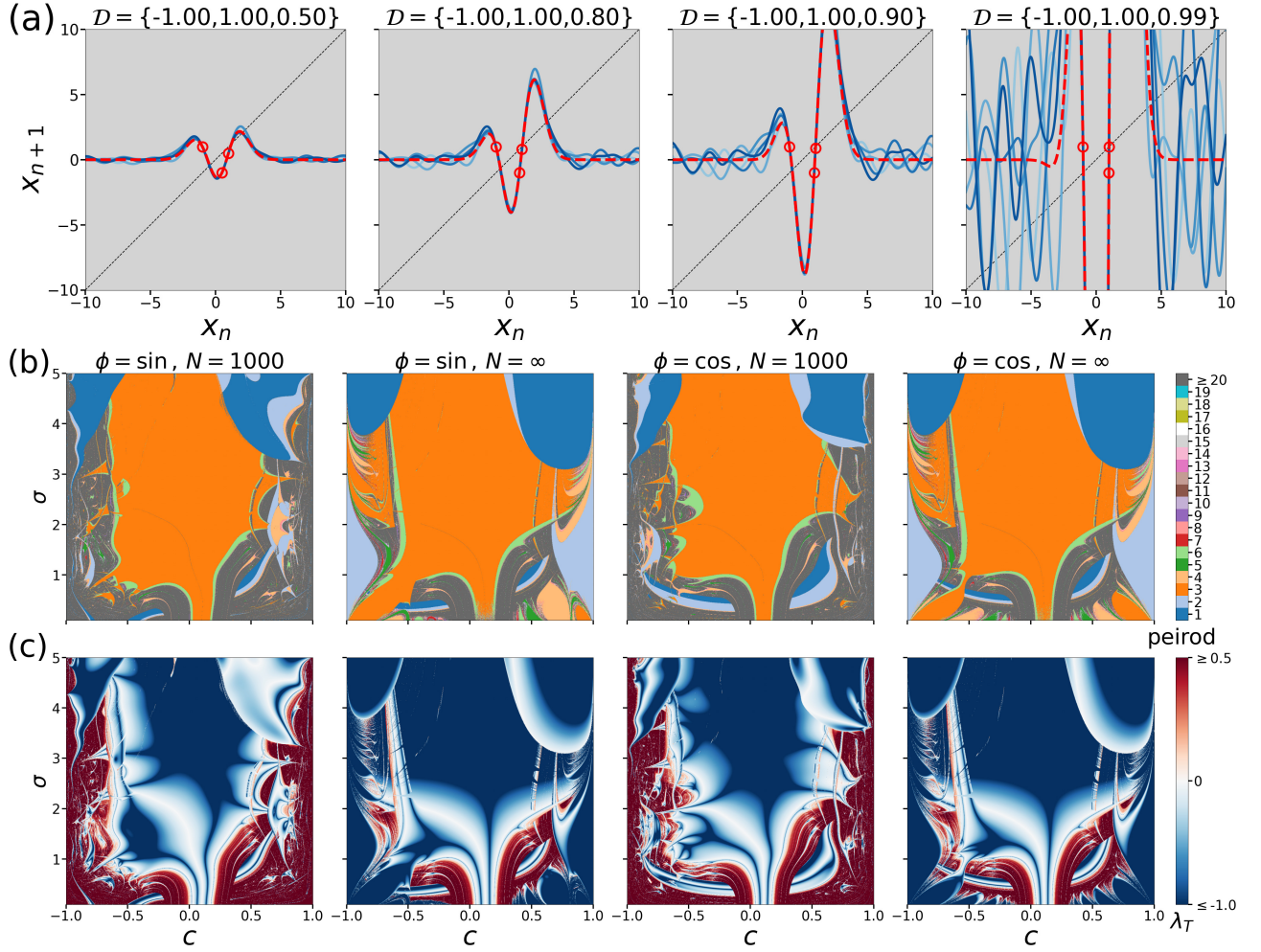


FIG. S10: Finite-size effects of learning machine for $\phi = \sin, \cos$ with $a = -1$, $b = 1$, and $N = 10^3$. (a) Trained maps f_N^* and f_∞^* for $\phi = \sin$ with $\sigma = 1.0$. The red circles and the red dotted lines show target period three and f_∞^* , respectively. The blue solid lines indicate five different realizations of f_N^* ; the wavy deviations of f_N^* from f_∞^* increase as c approaches a or b . (b),(c) Two-dimensional slices of the bifurcation structure of f_N^* and f_∞^* calculated with $x_0 = 0$, $T = 10^4$, and fixed realizations of the input layer.

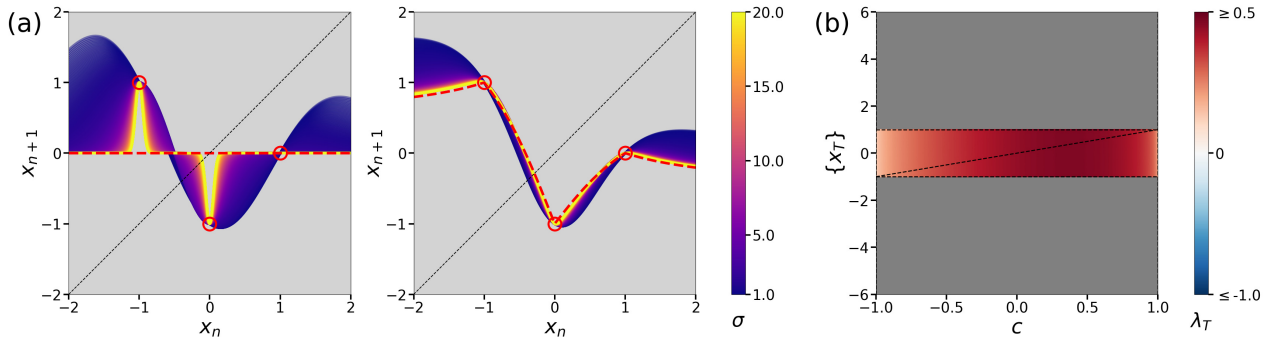


FIG. S11: Dynamical systems f_∞^* in the infinite input-intensity limit $\sigma \rightarrow \infty$ with $a = -1$ and $b = 1$. (a) Change in the map f_∞^* for $\phi = \sin$ (left) and erf (right) with respect to σ with $c = 0$ fixed. The red circles and the red dotted lines show the target period three and $\lim_{\sigma \rightarrow \infty} f_\infty^*$, respectively. (b) Bifurcation diagram of the characteristic attractors of $\lim_{\sigma \rightarrow \infty} f_\infty^*$ for $\phi = \text{erf}$ with respect to c calculated with $-10 \leq x_0 \leq 10$. In this limit, f_∞^* for $\phi = \text{erf}$ becomes piecewise-monotonic and piecewise-smooth, with target period three being its singular points; it exhibits the candidate of robust chaos in this setting.

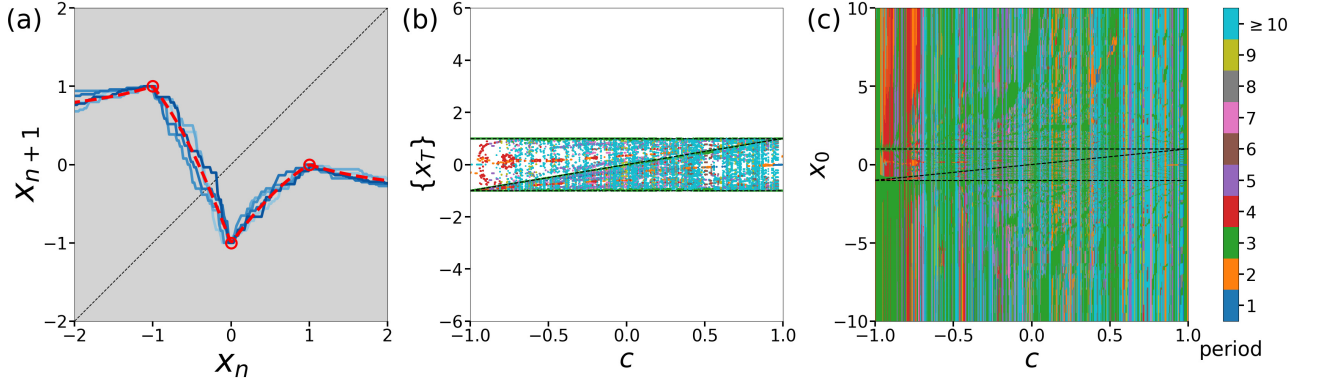


FIG. S12: Finite-size effects of learning machine for $\phi = \text{sgn}$ with $a = -1$ and $b = 1$. (a) Trained maps f_N^* and f_∞^* with $c = 0$ and $N = 100$. The red circles and the red dotted line show target period three and f_∞^* , respectively. The blue solid lines indicate five different realizations of f_N^* . (b) Bifurcation diagram of the attractors and (c) change in the basin of attraction calculated with $-10 \leq x_0 \leq 10$, $N = 10^3$, $T = 10^3$, and fixed realizations of the input layer. The complex structure in (c) corresponds to the discontinuity of f_N^* ; the dynamical systems properties of a trained network with $\phi = \text{sgn}$ qualitatively changes in its thermodynamic limit.

V. LEARNING PERIOD $n = 1, 2, 3, \dots$

In this section, we consider learning period $n = 1, 2, 3, \dots$ to investigate how the target period n affects the dynamical systems properties of learning machines. Assuming $\mathcal{D} = \{a_1, \dots, a_{n-1}, a_n\}$, we obtain the following formula of the

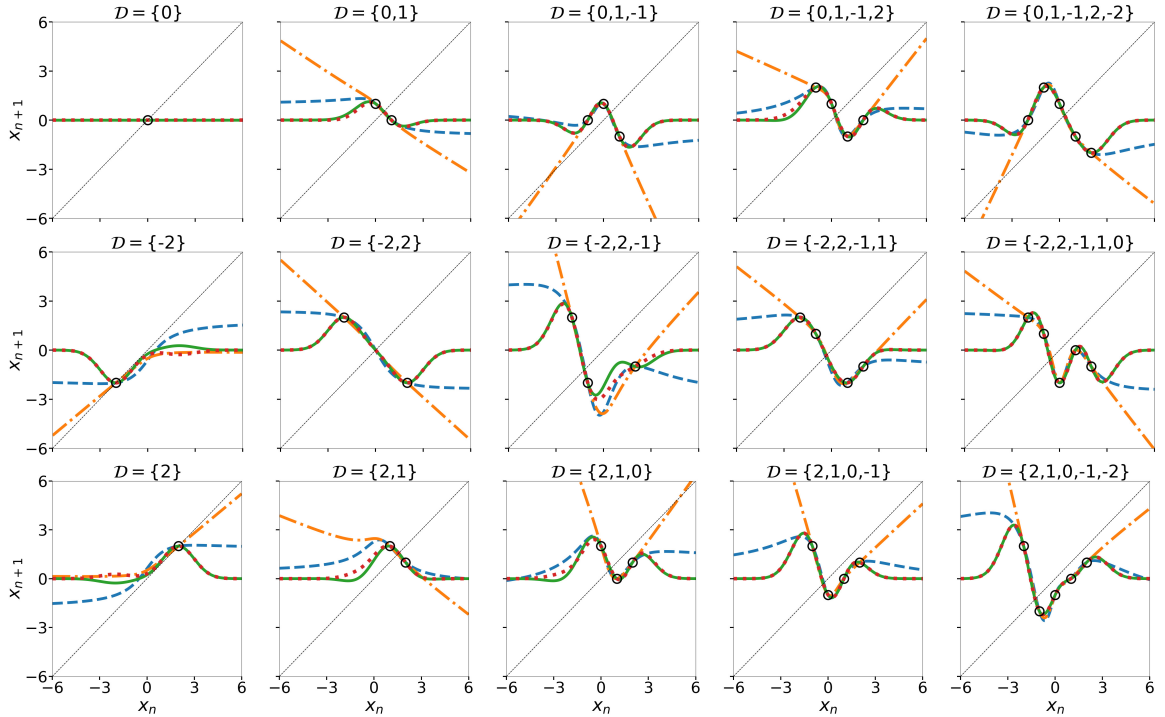


FIG. S13: Trained maps f_∞^* in learning period $n = 1, 2, 3, 4, 5$ with $\sigma = 1.0$ for $\phi = \text{erf}$ (blue line), \sin (green line), \cos (red line), and ReLU (orange line). Even in learning period $n = 1, 2$ (two leftmost columns), where there is only one type of \mathcal{D} , f_∞^* depends on the value of the target data. Increasing n explodes the number of types of \mathcal{D} , resulting in the strong dependence of f_∞^* on the ordering of periodic points in \mathcal{D} , as can be seen in the case of learning period $n = 5$ (rightmost column).

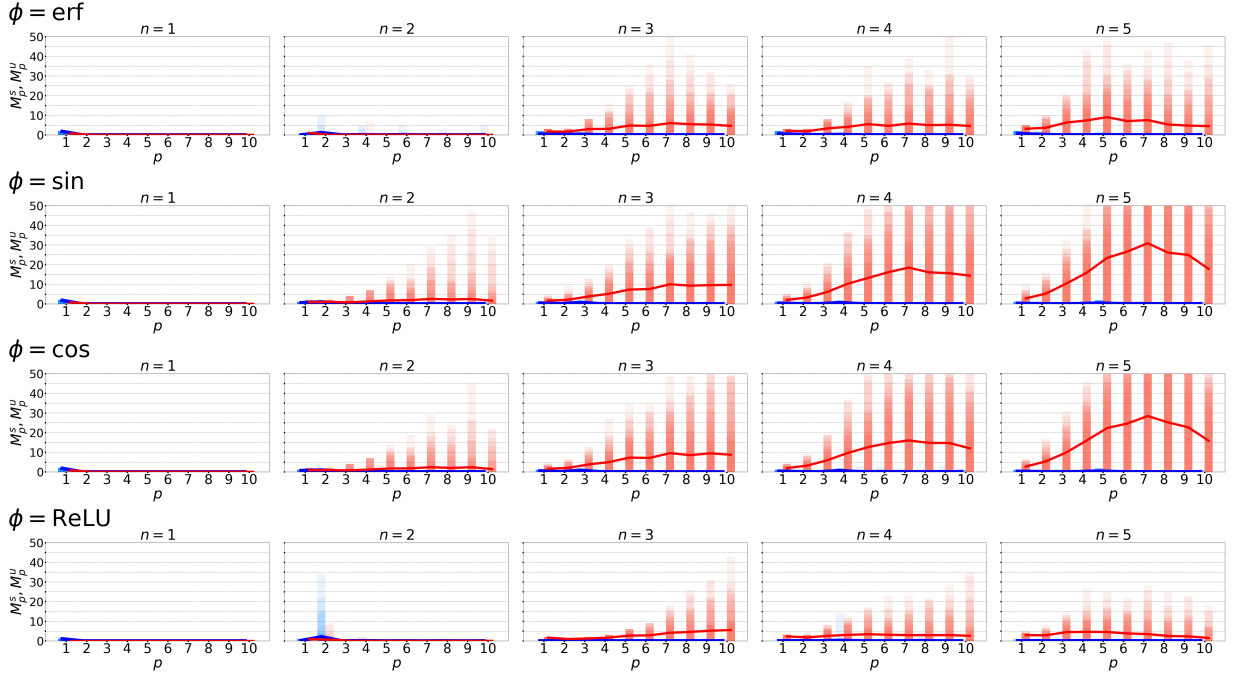


FIG. S14: Distribution of acquired periods in learning period n with $\sigma = 1.0$. Histograms for 100 different realizations of target data \mathcal{D} are overlaid for each n . The red and blue bins indicate the number of periodic orbits of period p with $S < 1$ (stable) and $S > 1$ (unstable), respectively. The solid lines show the average distributions of the acquired periods in learning period n . Periodic orbits of $S = 1$ were not detected in this setting.

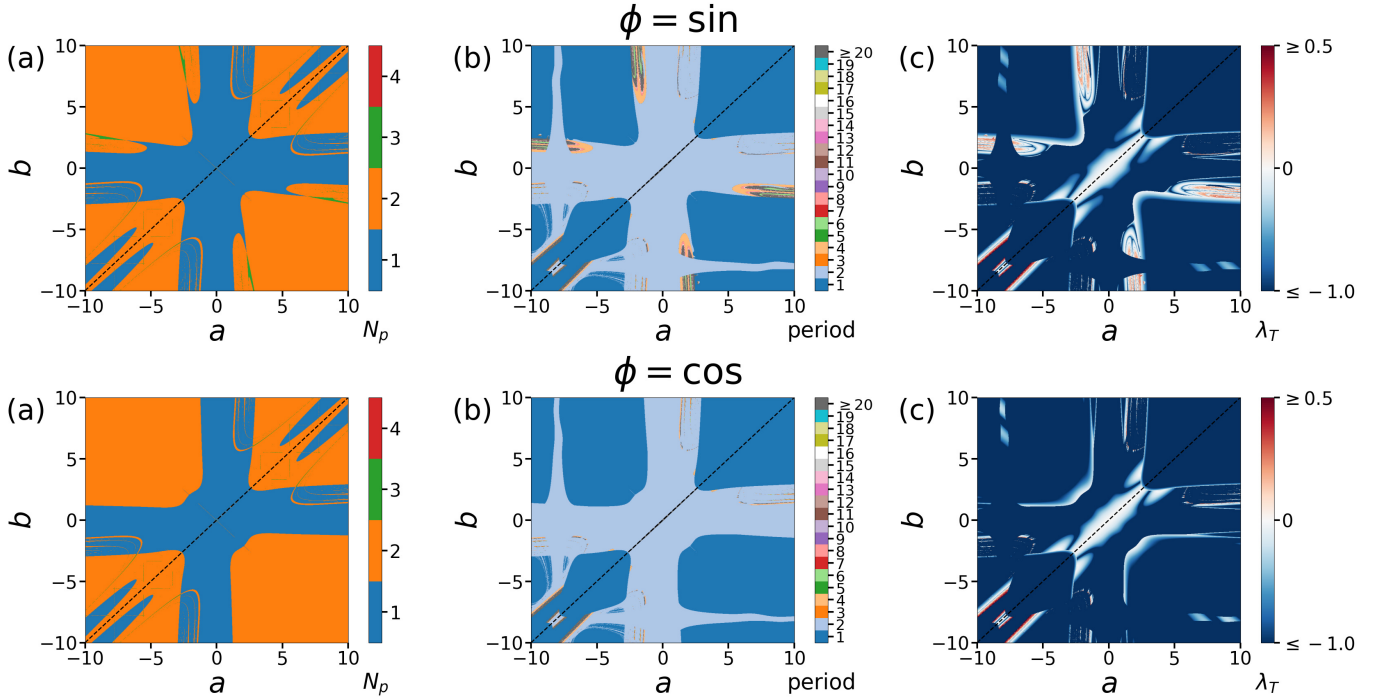


FIG. S15: Two-dimensional slices of the characteristic bifurcation structure of the dynamical system f_∞^* with respect to a and b , with $\sigma = 1.0$ and $T = 10^4$. (a) Number of kinds of period of attractors N_p calculated with 100 equidistant initial states in $-10 \leq x_0 \leq 10$. f_∞^* has roughly N_p attractors. (b) Period of attractors and (c) Lyapunov exponents calculated with $x_0 = -8$. The dotted lines represent $a = b$, and the bifurcation structure is symmetric about $a = b$ (Eq. (S65)).

trained network output in learning period n :

$$f_{\infty}^*(x) = [\Theta(x, a_1) \cdots \Theta(x, a_{n-1}) \Theta(x, a_n)] \begin{bmatrix} \Theta(a_1, a_1) & \cdots & \Theta(a_1, a_{n-1}) & \Theta(a_1, a_n) \\ \vdots & \ddots & \vdots & \vdots \\ \Theta(a_{n-1}, a_1) & \cdots & \Theta(a_{n-1}, a_{n-1}) & \Theta(a_{n-1}, a_n) \\ \Theta(a_n, a_1) & \cdots & \Theta(a_n, a_{n-1}) & \Theta(a_n, a_n) \end{bmatrix}^{-1} \begin{bmatrix} a_2 \\ \vdots \\ a_n \\ a_1 \end{bmatrix}. \quad (\text{S63})$$

Fig. S13 shows the examples of a trained map f_{∞}^* for $\phi = \text{erf}, \sin, \cos, \text{ReLU}$ in learning period $n = 1, 2, 3, 4, 5$. As n increases, the number of types of the target periodic orbit $(n-1)!$ explodes, making the shape of trained map more complex.

To investigate how n affects the acquired periods, we analyzed the periodic points of period $p = 1, 2, \dots, 10$ in the map f_{∞}^* with randomly drawn \mathcal{D} from the interval $[-10.0, 10.0]$ by solving the nonlinear equation

$$(f_{\infty}^*)^p(x) - x = 0 \quad (\text{S64})$$

using MATLAB `fsolve` command (Fig. S14). We uniformly chose 10^3 initial points from the interval $[-100.0, 100.0]$ to numerically solve Eq. (S64). To count the number of periodic orbits of period p , we used the absolute tolerance 10^{-2} to exclude the points belonging to the same periodic point, periodic orbit, and the periodic point of period $p' < p$ from the numerical solutions of Eq. (S64). We calculate the stability of the detected periodic orbit by computing $S \equiv |\frac{d}{dx}(f_{\infty}^*)^p(x)|$; we considered the periodic orbits of $S < 1$ to be stable and those of $S > 1$ to be unstable. We note that the average distribution of periodic orbits of f_{∞}^* is an universal property of the random network; however, it is affected by the tolerance 10^{-2} and the choice of the initial points in numerical calculations.

Fig. S14 indicates that regardless of the choice of ϕ , the number of unstable periods tends to increase dramatically after $n = 3$. This phenomenon may correspond to the fact that there always exists an appropriate ordering of period $n \geq 3$ that forces all periods (a Štefan sequence [18] of length 3), as discussed in Sec. 8 in Ref. [18]. Meanwhile, learning period two leads to non-trivial phenomena depending on the choice of $\mathcal{D} = \{a, b\}$ and ϕ . For $\phi = \text{ReLU}$, f_{∞}^* becomes like $f(x) = -x + \alpha$ ($\alpha \in \mathbb{R}$) for some choices of \mathcal{D} , resulting in a large amount of period-2 orbits (also see Fig. S13). For $\phi = \sin, \cos$, some choices of \mathcal{D} provide a large number of unstable periods in f_{∞}^* , thereby creating high-order periodic orbits, chaos, and multiple attractors in the characteristic bifurcation structure (Fig. S15). Note that in learning period two, f_{∞}^* is invariant under the swapping of a and b :

$$\begin{aligned} f_{\infty}^*(x)|_{\{a,b\}} &= \frac{1}{\Theta(a,a)\Theta(b,b) - \Theta(a,b)^2} [\Theta(x,a) \ \Theta(x,b)] \begin{bmatrix} \Theta(b,b) & -\Theta(a,b) \\ -\Theta(b,a) & \Theta(a,a) \end{bmatrix} \begin{bmatrix} b \\ a \end{bmatrix} \\ &= \frac{1}{\Theta(a,a)\Theta(b,b) - \Theta(a,b)^2} [\Theta(x,b) \ \Theta(x,a)] \begin{bmatrix} \Theta(a,a) & -\Theta(b,a) \\ -\Theta(a,b) & \Theta(b,b) \end{bmatrix} \begin{bmatrix} a \\ b \end{bmatrix} = f_{\infty}^*(x)|_{\{b,a\}}. \end{aligned} \quad (\text{S65})$$

-
- [1] A. Jacot, F. Gabriel, and C. Hongler, Neural tangent kernel: Convergence and generalization in neural networks, in *Advances in Neural Information Processing Systems*, Vol. 31, edited by S. Bengio, H. Wallach, H. Larochelle, K. Grauman, N. Cesa-Bianchi, and R. Garnett (Curran Associates, Inc., 2018).
 - [2] J. Lee, L. Xiao, S. Schoenholz, Y. Bahri, R. Novak, J. Sohl-Dickstein, and J. Pennington, Wide neural networks of any depth evolve as linear models under gradient descent, in *Advances in Neural Information Processing Systems*, Vol. 32, edited by H. Wallach, H. Larochelle, A. Beygelzimer, F. d'Alché-Buc, E. Fox, and R. Garnett (Curran Associates, Inc., 2019).
 - [3] A. Ali, J. Z. Kolter, and R. J. Tibshirani, A continuous-time view of early stopping for least squares regression, in *Proceedings of the Twenty-Second International Conference on Artificial Intelligence and Statistics*, Proceedings of Machine Learning Research, Vol. 89, edited by K. Chaudhuri and M. Sugiyama (PMLR, 2019) pp. 1370–1378.
 - [4] M. S. Advani, A. M. Saxe, and H. Sompolinsky, High-dimensional dynamics of generalization error in neural networks, *Neural Networks* **132**, 428 (2020).
 - [5] T. Liang and A. Rakhlin, Just interpolate: Kernel “ridgeless” regression can generalize, *The Annals of Statistics* **48**, 1329 (2020).
 - [6] T. Hastie, A. Montanari, S. Rosset, and R. J. Tibshirani, Surprises in high-dimensional ridgeless least squares interpolation, *The Annals of Statistics* **50**, 949 (2022).
 - [7] C. Williams, Computing with infinite networks, in *Advances in Neural Information Processing Systems*, Vol. 9, edited by M. Mozer, M. Jordan, and T. Petsche (MIT Press, 1996).
 - [8] Y. Cho and L. Saul, Kernel methods for deep learning, in *Advances in Neural Information Processing Systems*, Vol. 22, edited by Y. Bengio, D. Schuurmans, J. Lafferty, C. Williams, and A. Culotta (Curran Associates, Inc., 2009).
 - [9] M. Sahraee-Ardakan, M. Emami, P. Pandit, S. Rangan, and A. K. Fletcher, Kernel methods and multi-layer perceptrons learn linear models in high dimensions (2022), arXiv:2201.08082 [stat.ML].

- [10] C. Saunders, A. Gammerman, and V. Vovk, Ridge regression learning algorithm in dual variables, in *Proceedings of the 15th International Conference on Machine Learning, ICML'98* (Morgan Kaufmann, San Francisco, CA, 1998) pp. 515–521.
- [11] J. Suykens, Nonlinear modelling and support vector machines, in *IMTC 2001. Proceedings of the 18th IEEE Instrumentation and Measurement Technology Conference. Rediscovering Measurement in the Age of Informatics (Cat. No.01CH 37188)*, Vol. 1 (2001) pp. 287–294 vol.1.
- [12] M. Hermans and B. Schrauwen, Recurrent kernel machines: Computing with infinite echo state networks, *Neural Computation* **24**, 104 (2012).
- [13] W. De Melo and S. Van Strien, *One-Dimensional Dynamics* (Springer, Berlin, 1993).
- [14] S. v. Strien, T. Bedford, and H. Swift, Smooth dynamics on the interval (with an emphasis on quadratic-like maps), in *New Directions in Dynamical Systems*, London Mathematical Society Lecture Note Series (Cambridge University Press, 1988) p. 57–119.
- [15] S. Banerjee, J. A. Yorke, and C. Grebogi, Robust chaos, *Phys. Rev. Lett.* **80**, 3049 (1998).
- [16] S. Banerjee, M. Karthik, G. Yuan, and J. Yorke, Bifurcations in one-dimensional piecewise smooth maps-theory and applications in switching circuits, *IEEE Transactions on Circuits and Systems I: Fundamental Theory and Applications* **47**, 389 (2000).
- [17] J. Dong, E. Börve, M. Rafayelyan, and M. Unser, Asymptotic stability in reservoir computing, in *2022 International Joint Conference on Neural Networks (IJCNN)* (2022) pp. 01–08.
- [18] K. Burns and B. Hasselblatt, The sharkovsky theorem: A natural direct proof, *The American Mathematical Monthly* **118**, 229 (2011).